Reliability Engineering and System Safety 267 (2026) 111812

Contents lists available at ScienceDirect

Reliability Engineering and System Safety

journal homepage: www.elsevier.com/locate/ress

A novel multi-source sensor correlation adaptive fusion framework with uncertainty quantification for intelligent fault diagnosis[☆,☆☆]

Yue Yu [a], Hamid Reza Karimi [a,*], Len Gelman [b], Jinghui Tian [c], Peng Mei [d,e]

[a] Department of Mechanical Engineering, Politecnico di Milano, via La Masa 1, Milan 20156, Italy
[b] School of Computing and Engineering, University of Huddersfield, Queensgate, Huddersfield, HD1 3DH, UK
[c] Advanced Manufacturing Center, Ningbo Institute of Technology, Beihang University, Ningbo, 315800, China
[d] School of Transportation Science and Engineering, Beihang University, Beijing, 100191, China
[e] Department of Electrical, Electronic, Telecommunications Engineering and Naval Architecture, University of Genoa, Via Opera Pia 11a, Genova, 16145, Italy

ARTICLE INFO

Dataset link: https://github.com/Polimi-YuYue/Polimi-YuYue

Keywords:
Intelligent fault diagnosis
Uncertainty quantification
Dempster–Shafer evidence theory
Dirichlet distribution
Correlation adaptive

ABSTRACT

Intelligent fault diagnosis using multi-source sensor fusion holds significant promise but faces challenges related to reliability due to variations in signal quality across sensors and inconsistencies in fault features. To tackle these issues, a multi-source sensor correlation adaptive fusion (MSCAF) framework with uncertainty quantification is proposed to enhance identification trustworthiness for intelligent fault diagnosis. The proposed MSCAF integrates Dempster–Shafer theory with Dirichlet distribution to model sensor uncertainty and split multi-source sensors into high-confidence and low-confidence sensors based on the consistency of cross-sensor fault information. High-confidence sensors are given greater weight, ensuring more reliable fusion. Then, the reward and penalty functions are introduced to assess their correlation weights. Meanwhile, Convolutional and graph neural networks are employed to enhance feature extraction and output category probabilities, which can ensure robust fusion across varying diagnostic scenarios. This approach allows adaptive weighting, optimizes fusion reliability, and enables manual intervention for low-confidence sensors. Experimental results demonstrate that the proposed MSCAF achieves superior diagnostic performance compared to state-of-the-art methods, confirming its efficacy in extracting reliable features with uncertainty quantification for intelligent fault diagnosis.

1. Introduction

Mechanical equipment plays a vital role in modern industry, where its normal operation is essential for maintaining stability and efficiency in production processes [1–3]. By minimizing faults and downtime, the Prognostics and Health Management system (PHM) not only boosts productivity but also reduces maintenance costs, enhancing overall industrial performance [4–6].

With the rise of Industry 4.0 and the Internet of Things (IoT), intelligent fault diagnosis methods have gained popularity for their advanced feature extraction and identification capabilities within unified deep networks [7–9]. For example, Ding et al. proposed an interpretable multiplication convolution network (MCN) with analytically designed filtering kernels for efficient fault diagnosis [10]. Ma et al. [11] proposed a novel supply–demand deviation model based on Taguchi theory. This approach not only strengthens the mathematical foundation for analyzing communication networks but also fills a gap in understanding the coupling mechanisms between energy supply–demand deviation and communication bandwidth and power. Wang et al. proposed a dual-branch convolutional network with a multi-objective loss function to enhance early fault pulses in noisy vibration signals [12].

Although deep learning (DL)-based methods have made significant progress in mechanical fault diagnosis, uncertainty remains across all PHM tasks in industrial applications, potentially leading to decision-making errors in these methods [13,14]. Meanwhile, DL-based models function as black boxes, lacking interpretability, and produce deterministic classification results rather than probabilistic outputs for each category. Consequently, researchers in fault diagnosis often struggle to understand why traditional DL-based methods assign a particular diagnostic category over others or when to trust these diagnostic results fully. Unfortunately, traditional PHM methods, whether based

☆ This article is part of a Special issue entitled: ‘Uncertainty in PHM’ published in Reliability Engineering and System Safety.
☆☆ Source code can be available at: https://github.com/Polimi-YuYue/Polimi-YuYue.

* Corresponding author.
E-mail addresses: yue.yu@polimi.it (Y. Yu), hamidreza.karimi@polimi.it (H.R. Karimi), L.Gelman@hud.ac.uk (L. Gelman), jinghuitian@buaa.edu.cn (J. Tian), maple@buaa.edu.cn (P. Mei).

https://doi.org/10.1016/j.ress.2025.111812

Available online 27 October 2025

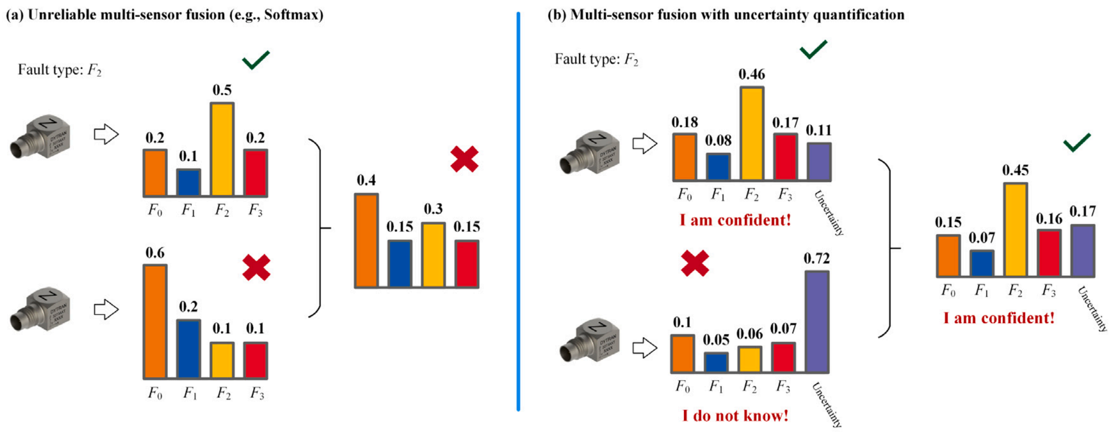

Fig. 1. Comparison of traditional DL-based methods and the proposed method incorporating uncertainty quantification.

on sensor data, physical knowledge, or a combination of both, are influenced by epistemic uncertainty, which can negatively impact PHM performance and undermine trust in intelligent fault diagnosis. For example, when a model trained on gearbox health conditions is exposed to motor or bearing conditions, it is often compelled to assign these unfamiliar cases to one of the known categories with high confidence, rather than expressing uncertainty or recognizing the input as unknown categories. Therefore, this oversight fails to alert users to the low reliability of such diagnostic results. In industrial applications, false confidence in misclassification can lead to inappropriate maintenance decisions or missed critical failures. Finally, uncertainty quantification in intelligent fault diagnosis is critical for advancing the state of the art in research and practice. It supports the development, validation, and confidence-building of PHM frameworks by incorporating uncertainty into diagnostic tasks, thereby enabling robust verification and validation of PHM solutions in alignment with decision-making requirements. Specifically, traditional methods typically employ the softmax function as the output layer and use its output as the predicted confidence. However, these approaches often result in high confidence for incorrect diagnostic outcomes, as the output probabilities sum to one, even when the sample does not belong to any category, as illustrated in Fig. 1(a). This issue restricts the broader application of DL-based methods for fault diagnosis in real industrial environments.

Generally speaking, reliable fault diagnosis requires accurate fault diagnosis, which can allow researchers to account for uncertainty quantification when these DL-based models fail. These approaches ensure reliable validation and confirmation of the developed solution in accordance with decision-use requirements. By assigning probabilities and uncertainties to different categories, these methods can enable more precise uncertainty quantification and allow for flexible integration of sensor data, physical knowledge, or their combination to support trustworthy decision-making, as shown in Fig. 1(b). Therefore, an optimal and robust fault diagnosis model should quantify the output uncertainty to ensure high diagnostic precision.

It is exciting that an increasing number of studies recognize the importance of uncertainty quantification in the fault diagnosis community, which can identify it as a promising direction in the field. Das et al. integrated assumed density filtering, heteroskedastic modeling, and Monte Carlo dropout in the uncertainty-aware framework to improve robustness and accuracy [15]. Zhao et al. proposed a simplified method for quantifying uncertainty to enhance model interpretability and enable human intervention [16]. Lu et al. proposed a clustering-based federated learning algorithm for fault diagnosis, which groups clients by dataset similarity using predictive uncertainty [17]. Zhang et al. introduced a trustworthy fault diagnosis method with out-of-distribution (OOD) detection for industrial systems [18].

Although most existing methods have made substantial contributions to uncertainty quantification, they still exhibit significant limitations when restricted to single-source sensor approaches. This is because, there is a significant diagnostic performance and scalability gap when processing single-source sensor data compared to multi-source sensor data fusion [19,20]. Meanwhile, multi-source sensor fusion methods in fault diagnosis are primarily implemented at the feature level. In multi-source sensor fusion, the most existing methods often assume that data collected by each sensor is equal, which means that each provides the same amount of fault information. This feature-level fusion approach implicitly assumes that the quality of each sensor remains consistent across all fault samples. However, these methods often need to be more accurate in sensor relevance for each fault sample, making them vulnerable to noise or irrelevant sensors in industrial environments. On the one hand, low-quality sensor data may be degraded by Gaussian white noise, unpredictable vibrations, or impacts. On the other hand, low-relevance sensors may lack valuable diagnostic features. Due to uncertainties in acquisition timing, experimental conditions, and machinery operational stages, the signal quality and relevance of sensors may vary across different fault samples. Traditional multi-source sensor fusion methods typically assume that the signal quality or importance of all sensors remains stable across all samples, which can assign equal or fixed weights to sensors at the feature fusion level. These approaches, however, are unsuitable for real industrial environments, as they often lead to diagnostic biases and limit practical applicability.

Uncertainty quantification through Dempster–Shafer (DS) evidence theory has inspired us to model the network output distribution as a Dirichlet distribution, which can lead to modifications in the DL-based framework [21,22]. In this paper, we proposed a novel multi-source sensors correlation adaptive fusion framework with uncertainty quantification for mechanical fault diagnosis. By leveraging multi-source sensor data, our proposed method dynamically adapted to the correlations between data collected by different sensors. We introduced DS evidence theory to quantify the uncertainty of fault information provided by each sensor. This work applies the DS theory by replacing the softmax function with the non-negative activation function (ReLU) to quantify and model the uncertainty of probabilities obtained from multi-source sensors through the proposed feature extractor. For practical applications in mechanical fault diagnosis, the sensor uncertainty measurement of DS theory is more feasible due to its significantly reduced computational complexity. Throughout this paper, the term ‘correlation’ will refer to the role of individual sensors in classification performance, which is determined by both the confidence level and the consistency between the data from each sensor and the corresponding fault information. To the best of our knowledge, this is the first attempt to quantify uncertainty in multi-source sensors fault diagnosis using category probabilities after feature extraction and to leverage this uncertainty for robust fault diagnosis. First, we propose a feature extractor that combines CNN and GCN to extract class probabilities from multi-source sensors, enhancing feature representation and class discrimination capability. We then split the multi-source sensors into low-confidence and high-confidence groups based on the consistency of fault information across sensors. Subsequently, reward and penalty functions are constructed to determine the weights of low-confidence and high-confidence sensors for reliable fusion on uncertainty quantification. In this way, we aim to develop a reliable multi-source sensor fusion mechanism for intelligent fault diagnosis, which can eliminate correlation differences or variances between multi-source sensors.

The main contributions of this work are summarized as follows.

(1) To address the uncertainty quantification of multi-source sensors in data-driven PHM models, this paper proposed a novel method for dynamically assessing the correlations among multi-source sensors and performing uncertainty quantification. This method can offer a promising tool for gaining user trust in DL-based fault diagnosis models.

(2) We split multi-source sensors into low-confidence and high-confidence groups and evaluate their corresponding weights for reliable fault diagnosis using the constructed reward and penalty functions.

The remainder of this work is organized as follows: Section 2 discusses related works about CNN, GCN, Dirichlet distribution, and uncertainty quantification. Section 3 constructs and describes the proposed MSCAF. In Section 4, three case studies test the diagnostic performance of the proposed MSCAF with uncertainty quantification. Section 5 contains various model discussions to validate the proposed method. The conclusion of this work is described in Section 6. Finally, the future studies are presented in Section 7.

2. Related works

2.1. Uncertainty quantification with multi-source sensors

After obtaining Dirichlet distributions from different sensors, we focus on quantifying their uncertainty to dynamically fuse them, thereby achieving reliable integration of multi-source sensors. Specially, Han et al. propose a trusted multi-view classification algorithm that dynamically integrates multiple views at the evidence level [23]. Zhang et al. designed a framework, which fuses vibration, current, and acoustic signals using graph convolution, Dirichlet distribution, and Dempster–Shafer theory to achieve accurate and noise-robust fault diagnosis [24]. Xu et al. fused view-specific evidence to make reliable and accurate multi-view predictions in IoT and industrial applications [25]. For example, with three classes, the concentration parameter of the Dirichlet distribution α is set to $[1.2, 1.2, 1.2]$, resulting in evidence value $e = [0.2, 0.2, 0.2]$. The corresponding diagram is shown in Fig. 2(a), which yields a uniform distribution on the simplex. Hence, the uncertainty mass μ is approximately equal to 1, which indicates no significant bias in the classification results, as the probabilities for each category are nearly equal. In contrast, α is $[41, 2, 2]$ and thus the strong evidence is obtained at $[40, 1, 1]$, as shown in Fig. 2(b). The distribution is sharp and concentrated in the bottom left vertex of a two-dimensional simplex (i.e., triangle). Finally, given that α is $[6, 6, 6]$, thus we have evidence value $[5, 5, 5]$, as depicted in Fig. 2(c). Although this distribution has stronger evidence for each category, it also results in lower uncertainty, which can accurately diagnose faults. To address the limitations mentioned above, a prior constraint based on Kullback–Leibler (KL) divergence is incorporated into the Dirichlet distribution to ensure a more effective fusion of multi-source sensors.

To better quantify the uncertainty of multi-source sensors, the Dirichlet distribution can be intuitively transformed into a simple 3-simplex (i.e., triangular prism), as illustrated in Fig. 3. Different categories of evidence can be represented as a regular tetrahedron with four vertices, that is, $(1, 0, 0, 0)$, $(0, 1, 0, 0)$, $(0, 0, 1, 0)$, and $(0, 0, 0, 1)$. The opinion with the belief mass and the uncertainty can be expressed as a point M inside the regular tetrahedron. Therefore, the uncertainty quantification under multi-source sensors can be mapped to a point ($\hat{u}$) at the bottom.

Therefore, the different diagnostic results obtained from traditional multi-source sensor fusion are viewed as different vertices on a simplex. This means that each sensor is assigned the same weight, which may give sensors with less diagnostic information higher confidence levels, thus impacting the final classification result. To address the issue mentioned above, uncertainty quantification is added in this paper. Hence, uncertainty quantification diagnostic results based on Dirichlet distribution can be regarded as the category probability of each vertex on a simplex. It means that we calculate the Dirichlet distributions of each sensor and combine them with the Dempster–Shafer theory (DS) to improve the reliability of the diagnostic results.

In DS, the Dirichlet parameter α_i is associated with the category evidence e_i produced by the DL methods, which can be expressed as

$$\alpha_i = e_i + 1 \tag{1}$$

where α_i means the class evidence, which assesses the level of support for diagnosing a sample as a specific fault category. Then, the uncertainty of multi-source sensors and the belief mass can be obtained by the subjective logic:

$$u = \frac{K}{S} \tag{2}$$

$$b_i = \frac{e_i}{S} \tag{3}$$

where S means the Dirichlet strength in Eq. (13), which can be shown as $S = \sum_{i=1}^{K} \alpha_i$. b_i represents the belief masses which evaluate the confidence of the kth category. The relationship between u and b_i is given as follows:

$$\sum_{i=1}^{K} b_i + u = 1 \tag{4}$$

It can be seen that parameters b_i and u form the basis for reliable diagnosis, which is consistent with Fig. 3. The less confidence b_i (a.k.a., evidence) collected by multi-source sensors, the higher the uncertainty u in fault diagnosis.

Finally, based on the subjective opinion mentioned above, the mean category probability with the Dirichlet distribution parameter u can be expressed as

$$p = \frac{\alpha_i}{S} \tag{5}$$

Traditional multi-source sensor fusion methods generally suffer from the limitations of fixed weight assignment and overconfident diagnostic results. Specifically, existing methods assume that each sensor contributes equally to the diagnostic results and assign fixed weights; however, in practice, the sensitivity of different sensors to faults varies significantly, and such a static fusion strategy is unable to dynamically adapt to changes in sensor significance between samples. Meanwhile, the Softmax output layer of traditional neural networks tends to produce excessive confidence and lacks effective quantification of prediction uncertainty. Therefore, in this study, the Dirichlet distribution is used to model the evidence for each sensor, and the concentration parameter $\alpha_i = e_i + 1$ is designed to ensure that the baseline level of support is maintained when there is insufficient evidence, while the model confidence is enhanced when there is sufficient evidence. Further, a simplified Dempster–Shafer theory of evidence is used to fuse joint evidence distributions from multiple sensors, achieving computational simplicity from 2^K complexity to linear complexity, while maintaining the transferability of evidence combinations. This theoretical framework not only dynamically quantifies the contribution weights of each sensor to the diagnostic results, but also effectively identifies out-of-distribution samples and provides plausible uncertainty estimates, thus significantly improving the reliability and robustness of multi-source sensor fault diagnosis.

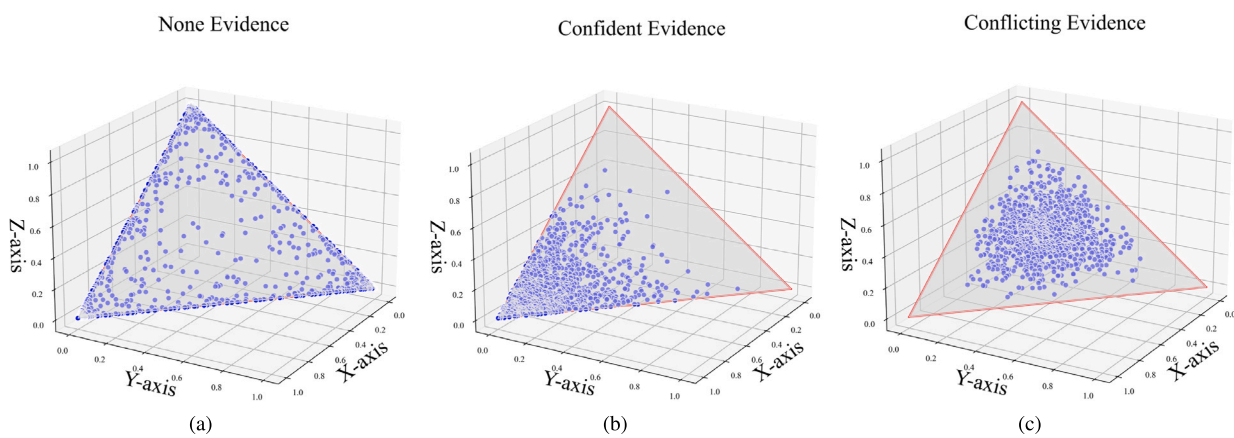

Fig. 2. Classical example of the Dirichlet distribution. (a) None evidence. (b) Confident evidence. (c) Conflicting evidence.

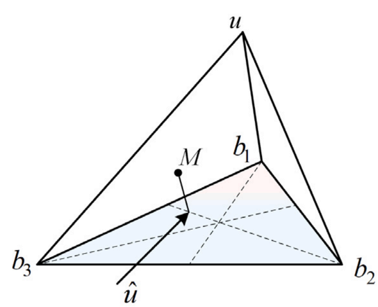

Fig. 3. Subjective opinion.

2.2. Convolutional Neural Network

The classical Convolutional Neural Network (CNN) has demonstrated significant success due to its robust local connectivity, parameter sharing, and feature learning capabilities. A typical CNN consists of a convolution layer, a pooling layer, a fully connected and an activation layer, as shown in Fig. 4 [26–28].

First, the convolution layer applies convolution operation to extract hierarchical features from the input data. Second, the pooling layer is used to mine valuable information further and reduce the computational load. Finally, the fully connected layer is utilized to perform classification or regression. Among them, the nonlinear activation function (i.e., Rectified Linear Unit, ReLU) is employed to equip CNN with better nonlinear feature learning ability. Therefore, the detailed operations can be obtained by the following equations:

$$y_{\mathrm{conv}}^{m+1} = \sigma\left(\sum_{i=1}^{N}\sum_{j=1}^{K} w_{i,j}^{m} * x_i^m + b_{i,j}^{m}\right) \tag{6}$$

$$y_{\mathrm{pool}}^{m+1} = \mathrm{pooling}_S\left(y_{\mathrm{conv}}^{m+1}\right) \tag{7}$$

where $\sigma(\cdot)$ and $\mathrm{pooling}_S(\cdot)$ refer to the activation function (e.g., Sigmoid) and pooling layer, separately. $w_{i,j}^{m}$ and $b_{i,j}^{m}$ stand for the weight and bias, respectively. x_i^m and y_{conv}^{m+1} represent the input and output feature map, separately. The CNN acts as a feature encoder to mine shallow features from multi-source sensors for node features and graph topology extraction by the subsequent GCN.

2.3. Spectral graph convolution

The quality of the graph data $G = \{V, A, E, F\}$ is essential to the Graph Convolution Network (GCN), which consists of the node set V, adjacency matrix A, edge set E, and feature matrix F, as shown in Fig. 5. Given that graph data $x \in \mathcal{R}^{N\times S}$, the output through spectral graph convolution can be expressed as

$$Y = g_{\theta_l} *_G x = U g_{\theta_l} U^T x \tag{8}$$

where g_θ and $*_G$ refer to the graph spectral filters and spectral graph convolution, respectively. θ_l is the learnable parameters. U means eigenvectors of symmetric normalized graph Laplacian matrix L, defined as:

$$L = I_N - D^{-1/2} A D^{-1/2} \tag{9}$$

where D and I_N stand for the diagonal degree matrix and identity matrix, respectively.

To further improve effectiveness and achieve globalization, Defferrard et al. [29] and Kipf and Welling [30] introduced Chebyshev polynomial expansion into the convolution kernel g_θ, written as

$$g_\theta \approx \sum_{k=0}^{K-1} \theta_{k_l} T_k(\tilde{\Lambda}) \tag{10}$$

with $\tilde{\Lambda} = 2\Lambda/\lambda_{\max} - I_N$, where $\lambda_{\max}$ means the maximum value of Λ K and $T_k(\tilde{\Lambda})$ refer to the order of Chebyshev polynomial expansion and diagonal element function, separately.

Therefore, the updated output Y of the spectral graph convolution can be expressed as follows:

$$Y = \sum_{k=0}^{K-1} \theta_{k_l} U T_k(\tilde{\Lambda}) U^T x \tag{11}$$

Finally, the output data $x' \in \mathcal{R}^{N\times M}$ of one GCN layer is expressed as

$$x' = \mathrm{Cheb}(x, w) = Y W_l \tag{12}$$

where $\mathrm{Cheb}(\cdot)$ and $W_l \in \mathcal{R}^{S\times M}$ refer to the Chebyshev graph convolution and learnable parameter, respectively.

2.4. Dirichlet distribution

The Dirichlet distribution generalizes the Beta distribution in a multi-dimensional space and is a non-parametric model [23,31]. It is a widely applied multivariate probability distribution in various fields, such as document identification, video classification, and polynomial regression. Given a parameter vector $\alpha = [\alpha_1, \ldots, \alpha_K]$, the probability density function based on Dirichlet distribution can be written as

$$\mathrm{Dirichlet}(\mu|\alpha) = \begin{cases} \dfrac{1}{B(\alpha)} \prod_{i=1}^{K} \mu_i^{\alpha_i - 1} & \text{for } \mu \in \Psi_K, \\ 0 & \text{otherwise.} \end{cases} \tag{13}$$

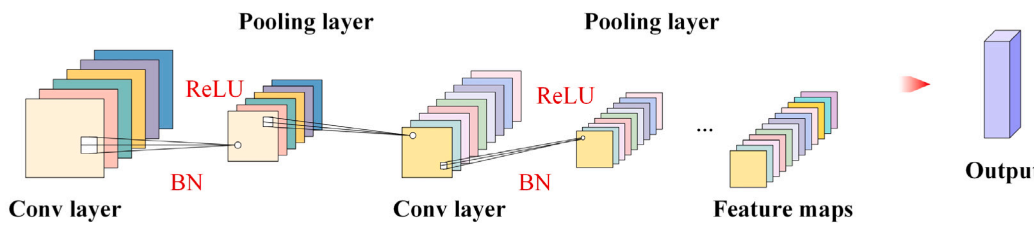

Fig. 4. Framework of convolutional neural network.

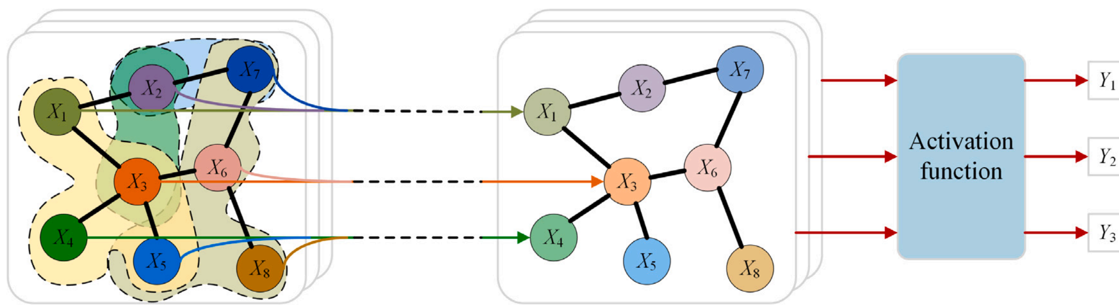

Fig. 5. Framework of graph convolutional network.

where $B(\alpha)$ and Ψ_K refer to the multivariate B function and the dimensional unit simplex, respectively, which are defined as follows:

$$\Psi_K = \left\{ \mu \mid \sum_{i=1}^{K} \mu_i = 1 \text{ and } 0 \le \mu_1, \dots, \mu_K \le 1 \right\} \tag{14}$$

$$\mathrm{B}(\alpha) = \frac{\prod_{i=1}^{K} \Gamma\left(\alpha_i\right)}{\Gamma\left(\sum_{i=1}^{K} \alpha_i\right)} \tag{15}$$

where $\Gamma(\cdot)$ represents the gamma function.

3. Proposed method

3.1. Problem formulation

As shown in Fig. 6, we presented the framework of the multi-source correlation adaptive fusion with uncertainty quantification to conduct mechanical fault diagnosis based on Dirichlet distribution, which consists of the feature extractor, the split of high-confidence/low-confidence sensors, and the reliable fusion on uncertainty quantification. In this paper, we first analyzed the limitations of traditional multi-source sensor fusion in fault diagnosis. We devised a solution by obtaining a correlation adaptive between prediction confidence and consistency of prediction results among multi-source sensors with Dirichlet distribution, which can be utilized to quantify the confidence of each sensor for the reliable fusion diagnosis. Given that the multi-source sensors data is written as $\left\{\left(S_i^1, S_i^2, \dots, S_i^K\right), y_i\right\}_{i=1}^{N}$, where N and K refer to the number of samples and sensors, respectively. The objective of this framework is to obtain the correlations of different sensors and to use adaptive weights for fusion, which can achieve a reliable fusion of multi-source sensors for fault identification y_i. Despite the success of existing multi-source sensor diagnostic methods, they face critical challenges in trustworthy fault diagnosis under uncertainty conditions. Traditional multi-source sensor fusion assumes fixed reliability across all samples: $\hat{y} = \sum_{m=1}^{M} w_m \cdot f_m(\mathbf{X}^{(m)})$ where w_m are static weights. However, in practical engineering scenarios, the reliability of each sensor varies significantly due to noise interference $\mathbf{X}^{(m)} = \mathbf{S}^{(m)} + \epsilon^{(m)}$, data quality degradation, and signal-specific sensitivity. The core challenge is to dynamically estimate sample-dependent uncertainty $u_i^{(m)} = \frac{K}{S_i^{(m)}}$ for each modality m and sample i, where $S_i^{(m)} = \sum_{k=1}^{K} \alpha_{i,k}^{(m)}$ represents the Dirichlet strength with concentration parameters $\boldsymbol{\alpha} i^{(m)} = e_i^{(m)} + \mathbf{1}$ derived from evidence $e_i^{(m)}$. Therefore, developing a trustworthy multi-source sensor fusion framework MSCAF is to access the correlation of each sensor dynamically and fuse them with adaptive weights, achieving a reliable fusion of sensors for intelligent fault diagnosis $\hat{y}$.

3.2. Feature extractor

First, the feature extractor based on CNN and GCN is proposed to output the probabilities from multi-source sensors as more reliable category evidence e. Specifically, the CNN in the feature extractor is first employed to extract features from the multi-source sensor signals. Subsequently, the Graph Construction Layer (GCL) generates the adjacency matrix A by performing matrix multiplication between the extracted feature matrix and its transpose, which can be shown as follows:

$$\begin{cases} \tilde{X} = \mathrm{CNN}(X) \\ A = \mathrm{normlize}\left(\tilde{X}\tilde{X}^T\right) \\ \bar{A} = \mathrm{Top} - k(\mathrm{A}) \end{cases} \tag{16}$$

where $\mathrm{normlize}(\cdot)$ denotes the normalization operator. A and $\bar{A}$ represent the adjacency matrix and the sparse adjacency matrix, respectively. After that, the GCN in the feature extractor is proposed to model the constructed instance graphs [24,32], which can be written as follows:

$$H^0 = \mathrm{MRFConv}\left(\mathrm{AXW}^0\right) \tag{17}$$

$$e = \mathrm{MRFConv}\left(\mathrm{AH}^0\mathrm{W}^1\right) \tag{18}$$

where W_0 and W_1 refers to the learnable weight matrix. The specific design of the feature extractor is described in Table 1.

In this paper, the traditional soft-max function is replaced by the rectified linear unit (ReLU) function to produce the negative output. Specially, ReLU enables sparse activation and preserves the original scale of the input, thereby avoiding the normalization effect introduced by Softmax and more faithfully retaining uncertainty information. For example, based on the definitions of the soft-max and ReLU functions, soft-max compresses all input values into the range $[0, 1]$, whereas ReLU avoids this normalization effect by preserving the original scale of the input and retaining more uncertainty information through sparse activation [33].

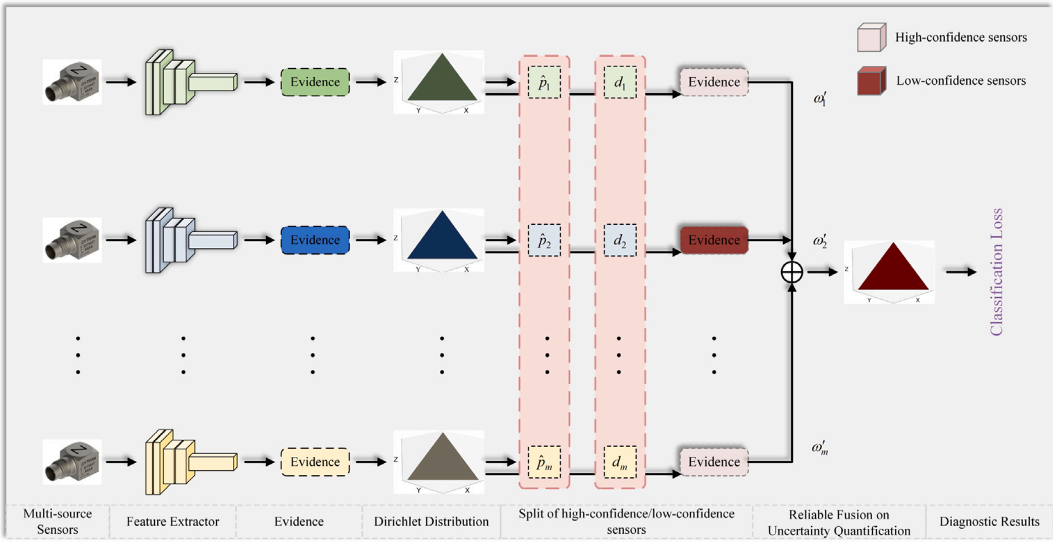

Fig. 6. Flowchart of the proposed method.

Table 1
Detailed structure of the feature extractor.

Component	Layer	Filter	Output size
Feature extractor	Input	/	$6\times32\times1024$
	Conv Layer_1	$16\times15\times1$	$6\times32\times16\times1010$
	Conv Layer_2	$32\times3\times1$	$6\times32\times32\times1008$
	Pooling_2	2×1 max-pool	$6\times32\times32\times504$
	Conv Layer_3	$64\times3\times1$	$6\times32\times64\times502$
	Conv Layer_4	$128\times3\times1$	$6\times32\times128\times500$
	Pooling_4	4×1 adaptive max-pool	$6\times32\times128\times4$
	Linear layer_4	512×256	$6\times32\times256$
	GCL	256×10	$6\times32\times32$
	GCN layer_1	256×400	$6\times32\times400$
	GCN layer_2	400×100	$6\times32\times100$
	Linear layer_2	100×256	$6\times32\times256$
Classifier	Linear layer_3	256×4	$6\times32\times6$

6 means the number of sensors.

3.3. Revisit the Dirichlet distribution in the proposed method

Most existing fault diagnosis methods input features extracted from original signals into a Softmax function to obtain class probabilities $\mu=[\mu_1,\dots,\mu_K]$, where $\sum_{k=1}^{K}\mu_k=1$. This is consistent with the parameters μ in the Dirichlet distribution. However, while the Softmax function effectively transforms logits into a probability distribution for fault diagnosis tasks, it often produces overconfident predictions due to its exponential nature and potential lack of calibration. We incorporated the Dirichlet distribution into the proposed method to address this limitation, obtain uncertainty, and alleviate the overconfidence problem.

3.3.1. Evidence lower bound

In this study, the samples originate from multi-source sensors and corresponding labels are denoted as $\mathbb{X}=\{x^l\}_{l=1}^{L}\in\mathbb{R}^{L\times H\times W}$ and $y\in\mathbb{R}^N$, where L, H, W, and N represent the number of samples, height of features, the width of features, and the number of labels, respectively. Meanwhile, the samples $x^l\in\aleph$ and labels $y\in Y$ belong to the sample domain $\aleph$ and the label domain Y, separately. For the single-source sensor, the generative process can be given as follows:

$$\begin{cases}\mu^m\sim p_{\theta^m}(\mu^m|x^m)=Dir(\mu^m|\alpha^m)\\ y\sim p(y|\mu^m)=Mult(y|\mu^m)\end{cases}\tag{19}$$

where $Dir(\cdot)$ and $Multi(\cdot)$ refer to the Dirichlet distribution and multinomial distribution, respectively. $\mu^m=[\mu_1^m,\dots,\mu_K^m]$ denote the class probabilities (a.k.a., multinomial distribution parameters). $p(y|\mu^m)$ is deduced from the feature extractor. $\alpha^m=[\alpha_1^m,\dots,\alpha_K^m]$ are the K concentration parameters. In contrast to the traditional Softmax function, which is prone to producing incorrect classification results with high confidence, the conjugate prior to the multinomial distribution is introduced to integrate data from multi-source sensors for more reliable diagnostic results.

To address the issue mentioned above, we further decompose the marginal likelihood $p_{\theta^m}(y|x^m)$. The following equations describe the detailed process:

$$\log p_{\theta^m}(y|x^m)=\mathcal{L}(x^m,y)+KL(q_{\theta^m}(\mu_m|x^m)\parallel p_{\theta^m}(\mu_m|x^m,y))\tag{20}$$

where $q_{\theta^m}(\mu_m|x^m)$ means the feature encoder with parameters θ^m. Then, $\mathcal{L}(x^m,y)$ can be transformed as follows [22]:

$$\mathcal{L}(x^m,y)=\mathrm{E}_{q_{\theta^m}(\mu^m|x^m)}[\log p(y|\mu^m)]-KL(q_{\theta^m}(\mu^m|x^m)\parallel p_{\theta^m}(\mu^m|x^m))\tag{21}$$

where $KL(\cdot)$ means the Kullback–Leibler divergence. Since the left side of Eq. (21) is a constant, the goal is to minimize the KL term. Given that KL divergence is always non-negative, we ultimately need to maximize the $\mathcal{L}(x^m,y)$. The second term $KL(q_{\theta^m}(\mu_m|x^m)\parallel p_{\theta^m}(\mu_m|x^m,y))$ in Eq. (21) is essentially the prior probability function to satisfy the Dirichlet distribution. Given a multi-class classification problem, the parameters of a given category μ_k associated with the ground truth label should be larger than the parameters μ_j for any other category j. This reflects the reasonable intuition that the prior distribution should favor the ground truth category more strongly, i.e., $\mu_k\gg u_j$. We modify the usual Softmax function to concentrate the Dirichlet distribution around the vertex corresponding to the ground truth label on a simplex. This idea tailors the Dirichlet distribution parameters to reflect a robust prior belief in the ground truth label. By using a non-negative activation function (i.e., Rectified Linear Unit (ReLU) and Softplus), adjusting the parameters for the ground truth label, and incorporating a KL divergence term, you ensure that the Dirichlet distribution is concentrated on the correct vertex of the simplex. This approach leverages prior knowledge to improve the multi-class fault diagnosis performance in the proposed framework. The detailed implementation process can be listed as follows:

$$e_i=\mathrm{FE}(\mathbb{X})\tag{22}$$

$$\alpha^m=\sigma(e_i)+1\tag{23}$$

$$\tilde{\alpha}^m=y+(1-y)\odot\alpha^m\tag{24}$$

where FE means the feature encoder. $\sigma(\cdot)$ denotes the non-negative activation function. y indicates a one-hot encoded vector representing the ground truth label. $\odot$ is element-wise multiplication. α^m and $\tilde{\alpha}^m$ refer to the Dirichlet distribution parameters and adjusted parameters, respectively, where the former parameters $[\alpha_1^m, \dots \alpha_K^m]$ should be greater than 1. The latter parameters $\tilde{\alpha}^m$ can avoid penalizing the Dirichlet parameter of the ground truth class to 1. the Correspondingly, the prior constraint can be expressed using the KL divergence between the obtained Dirichlet distribution and the uniform Dirichlet prior distribution:

$$D_{KL}\left[q_{\theta^m}(\mu^m \mid x^m) \parallel p_{\theta^m}(\mu^m \mid x^m)\right] \simeq D_{KL}\left[Dir(\mu^m \mid \tilde{\alpha}^m) \parallel Dir(\mu^m \mid [1, \dots, 1])\right] \tag{25}$$

where $\simeq$ means the isomorphism operation. Then, Eq. (25) can be further developed as follows:

$$\begin{aligned} D_{KL}\left[Dir(\mu^m \mid \tilde{\alpha}^m) \parallel Dir(\mu^m \mid [1, \dots, 1])\right] &= \log \frac{\Gamma(K)}{\Gamma\left(\sum_{k=1}^K \tilde{\alpha}_k\right)} \prod_{k=1}^K \frac{\Gamma(\tilde{\alpha}_k)}{\Gamma(1)} \\ &+ \sum_{k=1}^K (\tilde{\alpha}_k - 1)\left[\psi(\tilde{\alpha}_k) - \psi\left(\sum_{j=1}^K \tilde{\alpha}_j\right)\right] \\ &= \log\left(\frac{\Gamma\left(\sum_{k=1}^K \tilde{\alpha}_k\right)}{\Gamma(K)\prod_{k=1}^K \Gamma(\tilde{\alpha}_k)}\right) \\ &+ \sum_{k=1}^K (\tilde{\alpha}_k - 1)\left[\psi(\tilde{\alpha}_k) - \psi\left(\sum_{j=1}^K \tilde{\alpha}_j\right)\right] \end{aligned} \tag{26}$$

where $\Gamma(\cdot)$ and $\psi(\cdot)$ refer to the gamma function and digamma function, separately.

Finally, based on the equations presented above, the loss function for a single-source sensor is expressed as follows:

$$\mathcal{L}(x^m, y) = \mathbb{E}_{q_\theta(\mu^m \mid x^m)}\left[\log p(y \mid \mu^m)\right] - \lambda_t D_{KL}\left[Dir(\mu^m \mid \tilde{\alpha}^m) \parallel Dir(\mu^m \mid [1, \dots, 1])\right] \tag{27}$$

where λ_t is the trade-off parameter that balances the contributions between the two terms to avoid sub-optimal solutions.

3.4. Split of high-confidence/low-confidence sensors (SpS)

In real-world scenarios, we expect a more comprehensive integration of data from multi-source sensors to draw reliable diagnostic results. However, since Dempster–Shafer Theory (DST) tends to rely on high-confidence sensors overly, the final prediction may not sometimes align with what we intuitively consider reasonable. To tackle this issue, we proposed to split multi-source sensors into high-confidence/low-confidence sensors and evaluate their correlation with the reward and punishment functions, separately.

To obtain the different confidence levels of multi-source sensors, the average distance of each sensor in relation to other sensors is first calculated by the following equation:

$$d_{i,j} = \sqrt{\frac{1}{2}\left(\hat{p}_i - \hat{p}_j\right)^T \left(\hat{p}_i - \hat{p}_j\right)} \tag{28}$$

where $\hat{p}_i$ and $\hat{p}_j$ refer to class probabilities of the ith sensor and jth $(i \neq j)$ sensor, respectively.

Then, the average distance of the ith sensor is obtained by averaging the sum of distances between it and all other sensors, as given by

$$d_i = \frac{1}{M-1} \sum_{j \neq i} d_{i,j} \tag{29}$$

where M means the total quantity of multi-source sensors. d_i quantifies the degree of consistency in fault diagnosis with other multi-source sensors. The smaller the d_i, the greater the high-confidence of ith sensor in the multi-source sensors.

Finally, to further split the high-confidence and low-confidence sensors, the fault diagnosis consistency threshold θ can be defined as

$$\theta = \frac{1}{M} \sum_i d_i \tag{30}$$

where M means the number of multi-source sensors. If the average distance d_i is greater than the threshold θ, it signifies that this ith sensor conforms to the low-confidence.

3.5. Reliable fusion on uncertainty quantification

Based on the split of high-confidence/low-confidence sensors mentioned above, the reward and penalty functions $f_r\left(f_p\right)$ are introduced in this section to obtain further the correlation weights ω_i in conjunction with the uncertainty quantification of multi-source sensors. Therefore, these two functions can be written by the following equations:

$$f_r\left(S_i\right) = e^{-\bar{u}_i}, S_i \in S_{\text{high-confidence}} \tag{31}$$

$$f_p\left(S_i\right) = e^{-\left(1+\bar{u}_{\max}-\bar{u}_i\right)}, S_i \in S_{\text{low-confidence}} \tag{32}$$

with

$$\bar{u}_i = \frac{u_i}{\sum_i u_i} \tag{33}$$

where $\bar{u}_i$ means the normalized uncertainty quantification. To achieve reliable fusion of multi-source sensors, lower uncertainty quantification scores are assigned greater weights for high-confidence sensors to enhance evidence accumulation. In contrast, higher uncertainty scores receive greater weights for low-confidence sensors to minimize their impact on the final diagnostic results. Therefore, we can employ different reward and penalty functions based on sensor confidence levels, written as follows:

$$\omega_i = \begin{cases} e^{-\bar{u}_i} & \text{if } S_i = \text{True} \\ e^{-\left(1+\bar{u}_{\max}-\bar{u}_i\right)} & \text{if } S_i = \text{False} \end{cases} \tag{34}$$

where high-confidence sensors are marked as True. Then, to control the sensitivity of the weights and reduce fluctuations, we introduced a smoothing operation, which can be expressed as

$$\omega_i' = \frac{e^{\omega_i/\eta}}{\sum_{i=1}^M e^{\omega_i/\eta}} \tag{35}$$

where η means the temperature factor, which adjusts the sensitivity of the proposed method to changes in correlation, similar to adjusting the concentration of a probability distribution in a soft-max function. When η is small (e.g., close to 0), the distribution of weights becomes more concentrated, highlighting highly correlated weights. Conversely, when η is large, the weights become smoother, reducing their differences and decreasing instability caused by weight fluctuations. In this way, it can help the proposed method maintain more stable diagnostic results when faced with weight fluctuations among multi-source sensors, which can prevent excessive reliance on certain single weights. This is particularly important for multi-source sensors, as it reduces the impact of fluctuations in the correlation of individual low-confidence sensors on the overall method.

Finally, at a reliable confidence level, the robust fusion of high-confidence and low-confidence sensors is implemented, expressed as

$$e_f = \sum_i {\omega'}_i e_i \tag{36}$$

After that, the mean category probability $\hat{p}_f$ and the overall uncertainty quantification u_f of multi-source sensors can be obtained by Eqs. (5) and (2), separately.

3.6. Objective function

As mentioned in Section 3.3, the loss function based on single sensor can be expressed as

$$\mathcal{L}\left(x^{m}, y\right)=\mathbb{E}_{q_{\theta}\left(\mu^{m} \mid x^{m}\right)}\left[\log p\left(y \mid \mu^{m}\right)\right]-\lambda_{t} D_{KL}\left[Dir\left(\mu^{m} \mid \tilde{\alpha}^{m}\right) \| \ Dir\left(\mu^{m} \mid[1, \ldots, 1]\right)\right] \tag{37}$$

Therefore, the overall loss function for multi-source sensors can be accumulated as

$$L^{overall}=\sum_{k=1}^{K} \mathcal{L}(x^{m}, y) \tag{38}$$

To effectively model class probabilities in DS, the summation of the loss functions of multi-source sensors can be transformed into the integral of the traditional cross-entropy loss, which can be written as

$$\begin{aligned} L^{overall} &= \int L\left(x^{m}, y\right) dy=\int_{q_{\theta}\left(\mu^{m} \mid x^{m}\right)}\left[\log p\left(y \mid \mu^{m}\right)\right] dy \\ &-\lambda_{t} D_{KL}\left[Dir\left(\mu^{m} \mid \tilde{\alpha}^{m}\right) \| Dir\left(\mu^{m} \mid[1, \ldots, 1]\right)\right] \\ &= y\left(\psi\left(S_{i}\right)-\psi\left(\alpha_{ij}\right)\right)-\lambda_{t} D_{KL}\left[Dir\left(\mu^{m} \mid \tilde{\alpha}^{m}\right) \| \ Dir\left(\mu^{m} \mid[1, \ldots, 1]\right)\right] \end{aligned} \tag{39}$$

where $\psi(\cdot)$ means the digamma function, which is expressed as $\psi(x) = d\ln(\Gamma(x))/dx = \Gamma'(x)/\Gamma(x)$.

3.7. General flowchart

The General Flowchart of our MSCAF with uncertainty quantification to achieve mechanical fault diagnosis is illustrated in Fig. 7. Meanwhile, the specific procedure is listed as follows.

(1) *Step* 1: Collect multi-source sensor signals from three case studies.

(2) *Step* 2: Randomly sub-sample the multi-source sensor signals with a window length of 1024, then divide them into training samples and testing samples.

(3) *Step* 3: Employ the training datasets based on multi-source sensor signals to train the proposed MSCAF with the Adam optimizer.

(4) *Step* 4: Use the testing samples to test the diagnostic accuracy and efficiency of the proposed MSCAF with uncertainty quantification.

Finally, to clearly explain the proposed MSCAF, the overall loss function is optimized using the Adam optimizer during the backpropagation stage. The detailed procedure of the proposed MSCAF is presented in Algorithm 1.

Algorithm 1 The Proposed MSCAF

Input: Multi-source sensor data $\left\{\left(S_i^1, S_i^2, \ldots, S_i^K\right), y_i\right\}_{i=1}^{N}$.
Output: Diagnostic results y;
while not convergent **do**
  Randomly sample training datasets from Multi-source sensor data $\left\{\left(S_i^1, S_i^2, \ldots, S_i^K\right), y_i\right\}_{i=1}^{N}$.
  Input training datasets into the proposed feature encoder to obtain the class probabilities F in Eq. (22);
  Utilize the DS theory to model the distribution of each set of class probability F with the variational Dirichlet distribution, which can enable the extraction of class-wise evidence from multi-source sensors as described in Eq. (13).
  The mean category probability $\hat{p}_f$ and the overall uncertainty quantification u_f of multi-source sensors can be derived using Eqs. (5) and (2), separately.
  Split of high-confidence/low-confidence sensors in Eqs. (28), (29), and (30).
  Achieve reliable fusion on uncertainty quantification in Eqs. (31), (32), (33), and (35).
  Update the parameters of the proposed MSCAF by minimizing the objective function in Eq. (39).
end while
Obtain the final diagnostic results y.

Table 2
Test setup configuration of case study 1.

Components	
Active filters	Kemo PocketMaster 1600
Signal conditioner	Endevco Model 133
Data acquisition card	NI DAQCard-6062E
Laser speed sensor	DK10-LAS-54/76/110/124

Table 3
Description of health conditions in GCS.

Condition					
Million cycles	0–10	10–20	20–30	30–40	40–50
Label	0	1	2	3	4

4. Experimental verification

We use Python 3.12.4 and PyTorch 2.3.1 as DL frameworks in the three case studies. The hardware used includes an AMD Ryzen 7 5800H CPU with 16 GB of RAM and an NVIDIA GeForce RTX 3060 GPU with a compute capability 8.6. To ensure reproducibility and clarity, we explicitly define the hyperparameters of the Adam optimizer in the experimental setup, namely $\beta_1 = 0.9$, $\beta_2 = 0.999$, and $\epsilon = 10^{-8}$. All methods were repeated ten times to eliminate random errors in the following four case studies. **The code library is available at:** https://github.com/Polimi-YuYue/Polimi-YuYue.

4.1. Data descriptions

4.1.1. Case 1: Gearbox case study (GCS)

In this section, GCS based on the test rig produced by Newcastle University is built to diagnose early stage of pitting (i.e. micro-pitting) and test the diagnostic performance of MSCAF. Fig. 8 displays the general test rig used for run-to-failure experiments on the gearbox. The setup primarily consists of ① ② ③ accelerometers, ④ a proximity speed sensor, ⑤ a laser speed sensor, ⑥ a microphone, ⑦ a laptop running LabView software, ⑧ a D/A card, ⑨ a USB hard drive, and ⑩ a signal conditioner. This configuration is designed to generate and collect run-to-failure vibration signals under various operational cycles. Three accelerometers are mounted on the x-axis, y-axis, and z-axis of the gearbox to collect vibration signals at a sampling frequency of 40 kHz. A microphone is also positioned near the gearbox to capture sound data at the same sampling frequency, ensuring sufficient bandwidth for channel recording. The detailed data acquisition process is described in Fig. 9. In this case study, vibration and acoustic signals are recorded using three mono-axial accelerometers (KCF-107) positioned along three orthogonal directions, and a microphone (G.R.A.S. 40BI). Meanwhile, the test setup configuration is described in Table 2. Five health conditions under different operating cycles of the gearbox are considered, as described in Table 3 and Fig. 10. For simplicity, different labels are assigned to the health conditions.

We designed training and testing samples with different ratios to verify the generalization performance of the proposed method and other state-of-the-art (SOTA) methods as the training sample sizes change, as given in Table 4. Each data sample from multi-source sensors is constructed using a window length of 1024 consecutive points without overlaps during the segmentation process.

4.1.2. Case 2: Rolling Mill Case Study (RMCS)

The multi-source signals of the rolling mill collected from Yanshan University (YSU), China, are designed to verify the effectiveness and superiority of our method, as displayed in Fig. 11. The test rig consists of ① an induction motor, ② a coupling unit, ③a reduction gearbox,

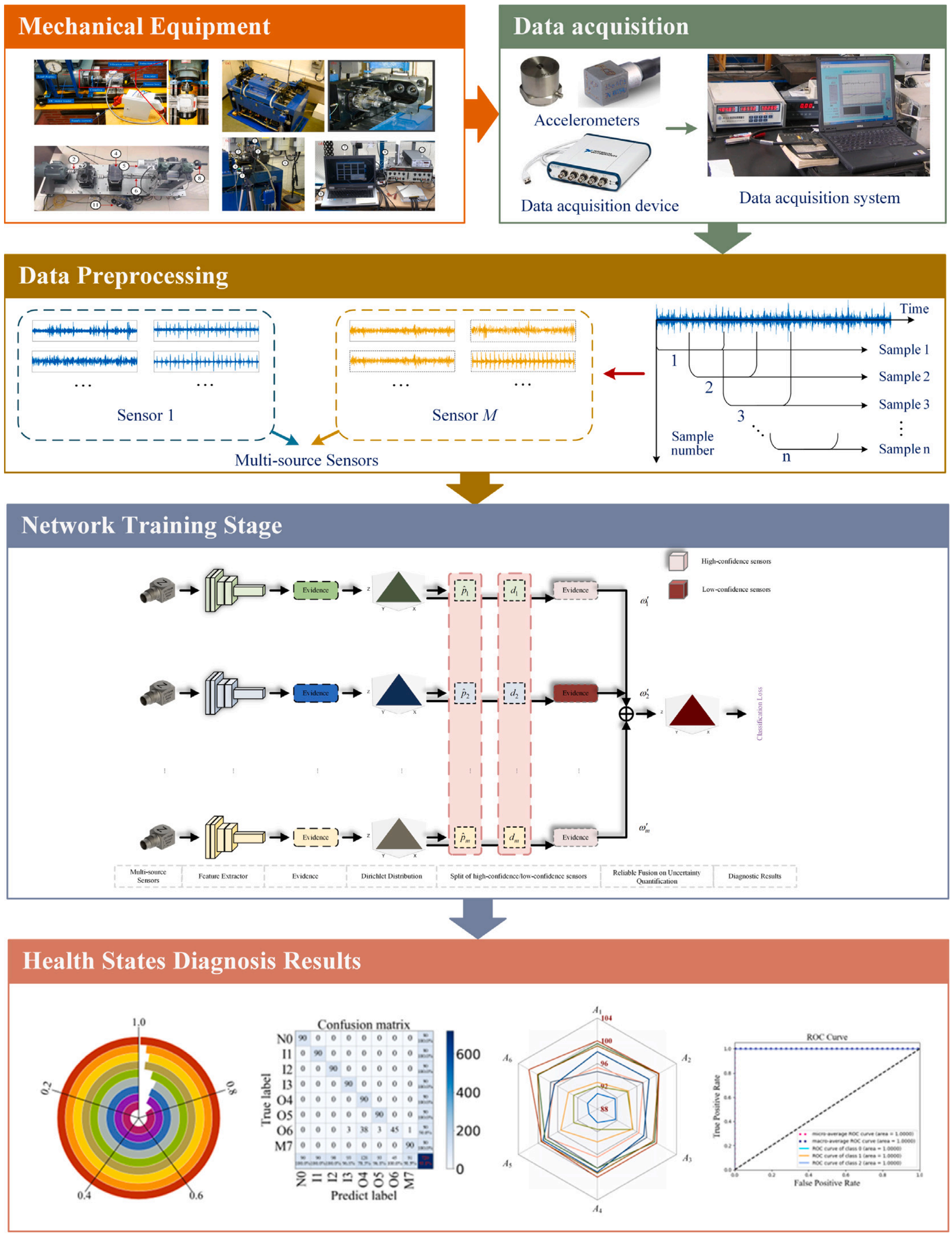

Fig. 7. Overall Framework.

Table 4
Detailed information on different datasets in GCS.

Different datasets	Training size	Testing size
Dataset 1	100	100
Dataset 2	50	100
Dataset 3	20	100

④ a direction-changing gearbox, ⑤ a cross universal joint, ⑥ a drive motor, ⑦ four rolls, ⑧ a hand-wheel, ⑨ one vertical shaker, ⑩ one horizontal shaker, and ⑪ a data acquisition system. In this experiment, four different health conditions of the bearing located in the housing of the lower work roll are simulated under three distinct rotational speeds: 10 Hz, 11.67 Hz, and 13.33 Hz. These conditions include normal condition (NC), inner race fault (IRF), outer race fault (ORF), and scroll element fault (SEF) as represented in Table 5 and Fig. 12. The six accelerometer sensors are installed on the following components: the side above the rolling mill stand, the upper backup roll, the upper work roll, the lower work roll, the lower backup roll, and the side below the mill stand, as depicted in Fig. 13. The multi-source sensor data are collected using an NI USB-4431, a portable data acquisition device, as shown in Fig. 14. The multi-source sensors used are a lightweight (1.0 g), miniature, ceramic shear ICP® triaxial accelerometer (Model No. PCB 3456A01) with a nominal sensitivity of 5 $\mathrm{mV/g}$ (±20%), equivalent to 0.51 $\mathrm{mV/(m\ s^2)}$, and a measurement range of ±1000 gpk. Meanwhile, the sampling frequency of the multi-source sensors was set

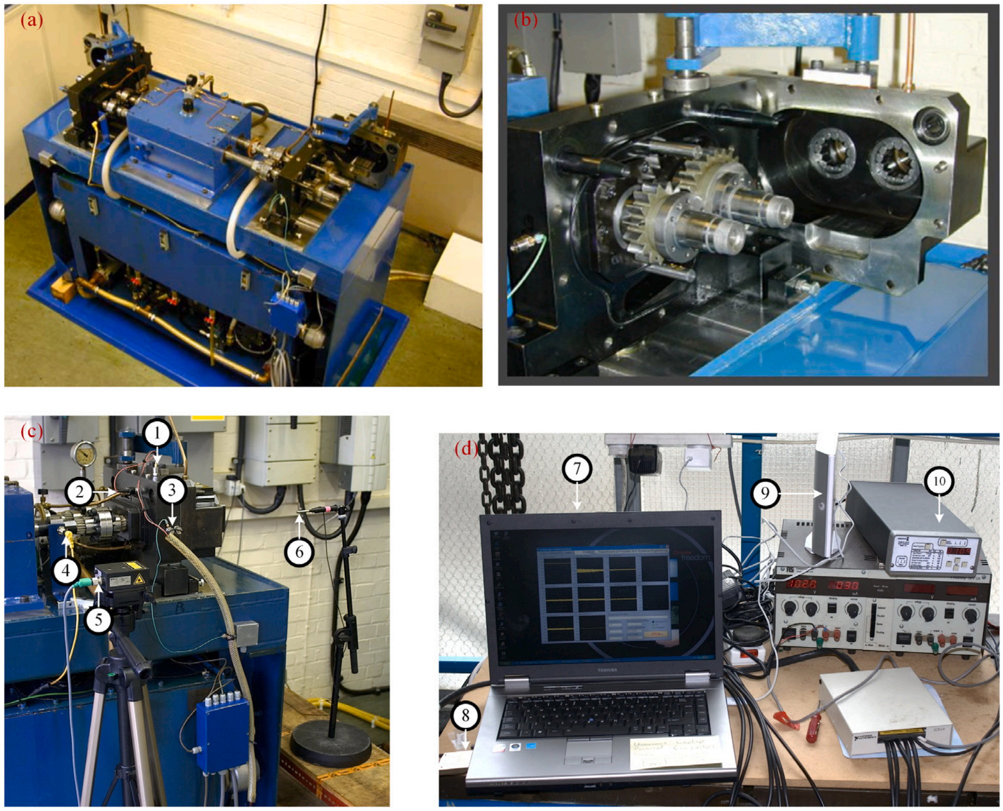

Fig. 8. General test rig of gearbox at Newcastle University. (a) test rig; (b) gearbox; (c) test setup configuration; (d) data acquisition system.

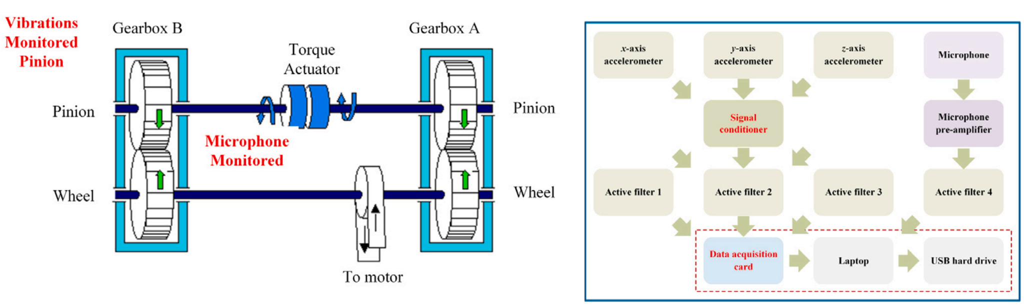

(a) (b)

Fig. 9. Experimental setup. (a) data acquisition location; (b) data acquisition flowchart.

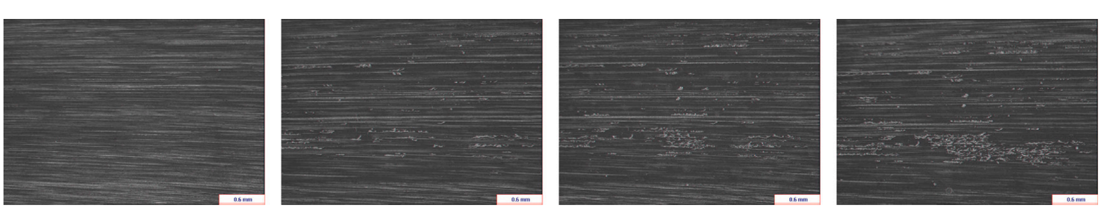

(a) (b) (c) (d)

Fig. 10. Five health conditions of the gearbox. (a) as ground; (b) after 10 million cycles; (c) after 30 million cycles; (d) after 50 million cycles.

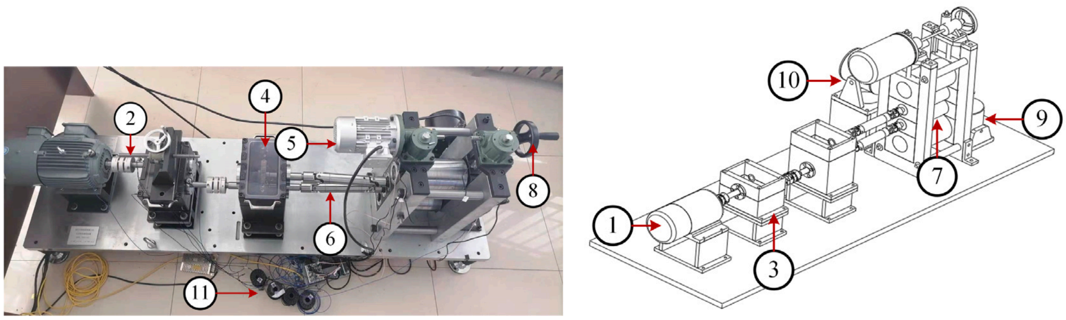

(a) (b)

Fig. 11. Test rig in RMCS. (a) typical photograph; (b) mechanical drawing.

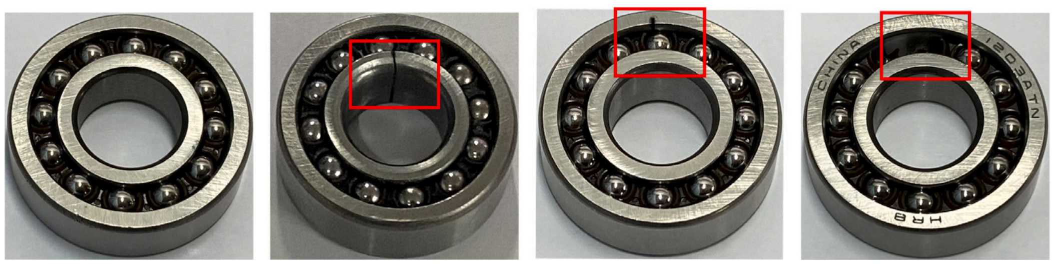

(a) (b) (c) (d)

Fig. 12. Bearing faults in RMCS. (a) NC; (b) IRF; (c) ORF; (d) SEF.

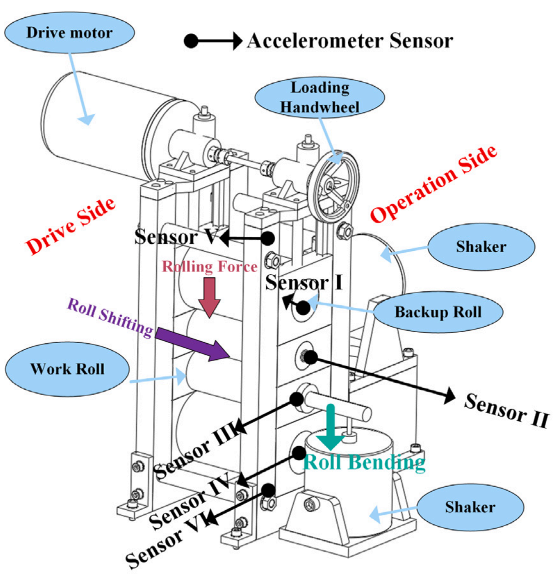

Fig. 13. Detailed locations of multi-source sensors in RMCS.

Table 5
Descriptions of health conditions in RMCS.

Condition	NC	IRF	ORF	SEF
Position	/	Inner race	Outer race	Scroll element fault
Label	0	1	2	3

to 10,240 Hz, and the point duration of the subsamples was set to 1024 without overlaps.

In this case study, to further validate the robustness of the proposed ECAMSF, the diagnostic performance of all methods at three rotating speeds is discussed, as given in Table 6. For each rotating speed, the number of training and testing datasets is designed as 200 and 100, separately.

Fig. 14. A typical photograph of data acquisition.

Table 6
Detailed information on different datasets in RMCS.

Different datasets	Rotating speed	Training size	Testing size
Dataset 4	10 Hz	200	100
Dataset 5	11.67 Hz	200	100
Dataset 6	13.33 Hz	200	100

4.1.3. Case 3: Motor Operating Case Study (MOCS)

Fig. 15 depicts the motor operating platform, consisting primarily of a load display, a DC motor loader, a current supply, a coupling, an induction motor, an encoder, a sensor box, and vibration sensors. A total of six different health conditions were conducted, including an outer race fault, an inner race fault, and a bearing ball with two different fault severity, as described in Table 7 and Fig. 16. The detailed data acquisition flowchart can be given in Fig. 17, and the sampling frequency was set to 40,960 Hz. In this experiment, motor loads were set to 0%, 40%, and 80%, as demonstrated in Fig. 18, to create three different datasets for verifying generalization performance, as shown in Table 8. Three vibration sensors (PCB 352C34) and two current sensors (Hioki CT6700) were employed to collect multi-sensor signals. For each

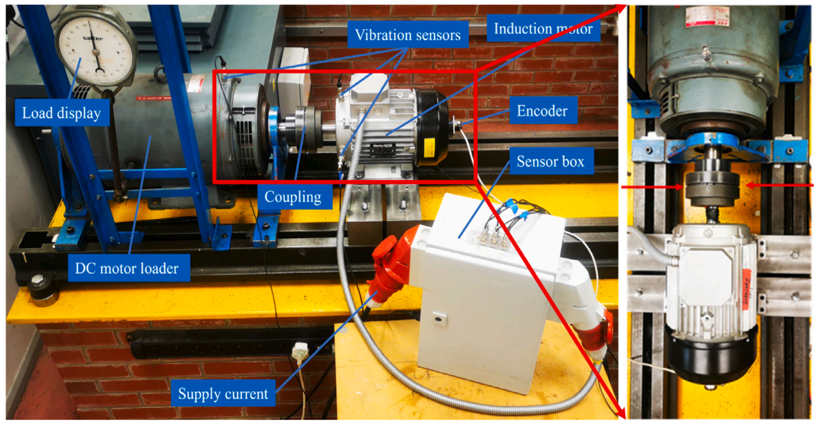

Fig. 15. Motor operating platform.

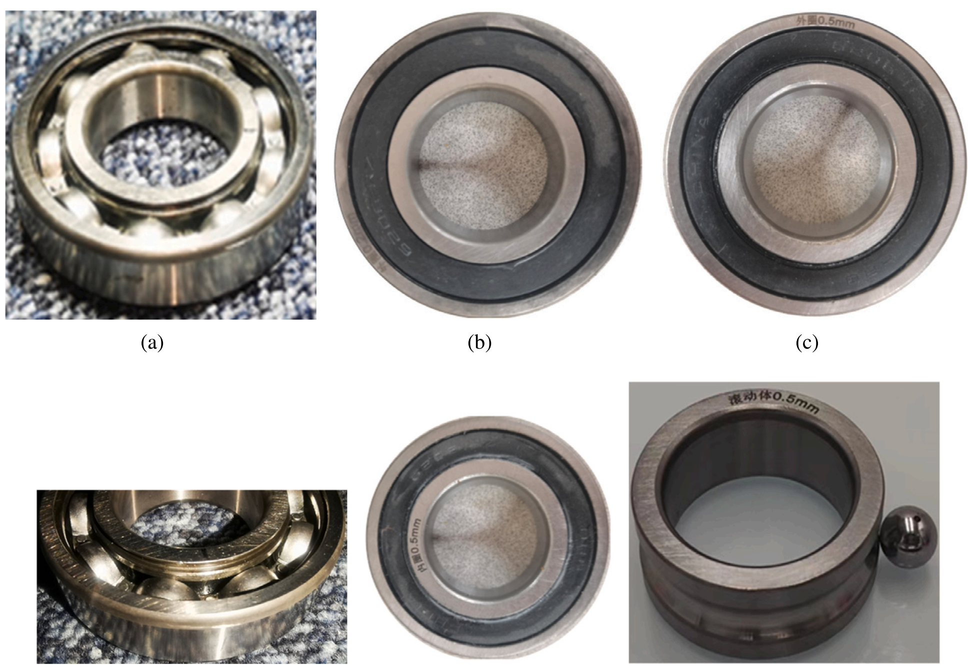

(a) (b) (c)

(d) (e) (f)

Fig. 16. Descriptions of health conditions in MOCS. (a) N0; (b) O1; (c) O2; (d) I3; (e) I4; (f) B5.

Table 7
Descriptions of health conditions in MOCS.

Condition	N0	O1	O2	I3	I4	B5
Severity (mm)	/	0.2	0.5	0.2	0.5	/
Position	/	Outer race	Outer race	Inner race	Inner race	Bearing ball
Label	0	1	2	3	4	5

Table 8
Detailed information on different datasets in MOCS.

Different datasets	Rotating speed	Training size	Testing size
Dataset 7	0%	200	100
Dataset 8	40%	200	100
Dataset 9	80%	200	100

dataset, the training and testing datasets were set to 200 and 100, respectively, with a data length of 1024 (see Fig. 18).

4.2. Implementation details and comparative methods

To assess and contrast the classification accuracy and efficiency of the proposed MSCAF with other SOTA methods, including single-source methods, traditional multi-source sensor fusion methods, and intelligent multi-source sensor fusion methods, the detailed information is provided as follows.

(1) The proposed MSCAF.

(2) DBN. The traditional DBN consists of three Restricted Boltzmann Machines (RBMs) with neuron sizes of 1024, 512, and 218, respectively.

(3) MSIDBN [34]. MSIDBN leverages multi-sensor information fusion and an improved deep belief network (DBN) to enhance diagnostic accuracy.

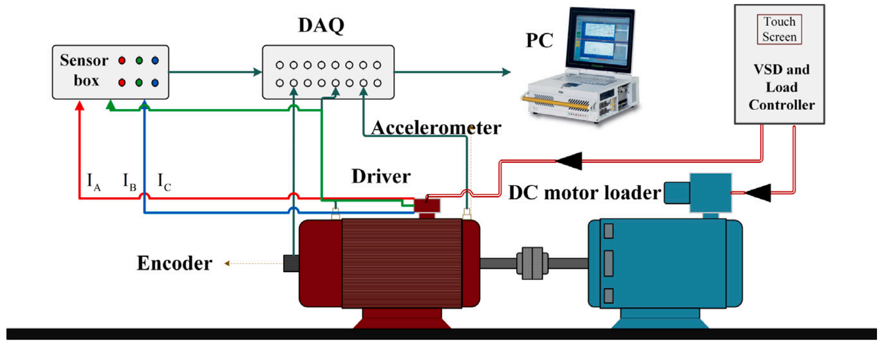

Fig. 17. Detailed locations of multi-source sensors in MOCS.

Fig. 18. Schematic diagram of three experimental motor loads in MOCS. (a) 0%; (b) 40%; (c) 80%.

(4) MSICNN [35]. MSICNN combines improved CNN and multi-source sensing data fusion to detect rolling mill health states.

(5) IMGCN [36]. IMGCN employs multi-channel data to enhance feature extraction and diagnostic performance

(6) CVC-Net [37]. CVC-Net employs adaptive convergent viewable neural networks, which can leverage multi-sensor fusion to achieve effective fault diagnosis.

(7) A-TSGNN [38]. A-TSGNN introduces an attention-aware temporal-spatial graph neural network, designed to capture dynamic temporal and spatial dependencies for integrating multi-sensor information fusion.

(8) MCFormer [39]. MCFormer utilizes a multi-branch Transformer-based architecture to address multi-sensor heterogeneity and enable intelligent feature fusion.

(9) I^{2}SGCN [40]. I^{2}SGCN introduces a two-stage subgraph convolutional network based on importance-aware analysis, which can utilize multi-source sensor data for fault diagnosis.

4.3. Diagnosis results

The diagnostic accuracy for three case studies is given in Table 9, and their corresponding histograms are shown in Fig. 19.

The striking results to emerge from the data are shown as follows:

(1) The proposed MSCAF achieves the highest average diagnostic performance across nine tasks and multi-source sensors with uncertainty quantification methods (i.e., CVC-Net, A-TSGNN, MCFormer, and I^{2}SGCN) outperform traditional multi-source sensor fusion approaches (i.e., MSIDBN, MSICNN, and IMGCN). Especially, the proposed method is 4.86%, 1.9%, 1.89%, 1.83%, 1.16% 1.43%, 1.43%, 0.95%, and 0.84% higher than DBN, MSIDBN, MSICNN, IMGCN, CVC-Net, A-TSGNN, MCFormer, and I^{2}SGCN, separately.

(2) This indicates that dynamically assessing sensor correlations with uncertainty quantification is highly effective for multi-source sensor fusion in diagnosing the health conditions of mechanical equipment. Conversely, assigning equal importance to all sensors, particularly those with low confidence, may degrade recognition performance due to the influence of unreliable sensors.

(3) Compared with the single-source DBN, the superior diagnostic accuracy of the multi-source sensor fusion methods can be attributed to their integration of complementary information from different signals, which enhances feature representation and enables more effective fault diagnosis.

4.4. Feature visualization via t-SNE

In this section, t-distributed Stochastic Neighbor Embedding (t-SNE) is used to visualize high-dimensional data in a low-dimensional space, which can further highlight the strengths and limitations of various methods. We take Dataset 6 as an example of feature visualization; the detailed results of all the methods can be represented in Fig. 20.

As illustrated in Fig. 20, the distinct features of the categories across all methods are clearly separated into five distinct regions. However, compared to comparative methods, the features learned from the proposed MSCAF are better well-aligned. The visualization results demonstrate that our proposed method effectively learns representative and discriminative features. These features are crucial for performing reliable mechanical fault diagnosis with uncertainty quantification under multi-source sensors.

4.5. Model diagnosis performance

First, to explore the diagnostic and effectiveness performance, a confusion matrix is used to construct the true and predicted labels in a tabular format. From the confusion matrix, five metrics can be introduced to assess model performance, namely accuracy, precision, recall, F1 score, and specificity, written as follows:

$$\text{Accuracy} = \frac{TP + TN}{TP + TN + FP + FN} \tag{40}$$

$$\text{Precision} = \frac{TP}{TP + FP} \tag{41}$$

$$\text{Recall} = \frac{TP}{TP + FN} \tag{42}$$

$$F1 = 2 \times \frac{\text{Precision} \times \text{Recall}}{\text{Precision} + \text{Recall}} \tag{43}$$

$$\text{Specificity} = \frac{TN}{TN + FP} \tag{44}$$

Table 9
Experimental results of different methods on the three case studies. Results are shown in form of [Mean ± Std]%.

Tasks	Accuracy (%)								
Dataset 1	95.48 ± 0.49	98.61 ± 0.39	98.73 ± 0.37	98.69 ± 0.36	98.92 ± 0.37	99.06 ± 0.32	99.14 ± 0.34	99.11 ± 0.33	**99.42 ± 0.27**
Dataset 2	87.93 ± 0.81	95.19 ± 0.46	95.81 ± 0.49	95.73 ± 0.42	95.83 ± 0.49	96.04 ± 0.42	96.29 ± 0.41	96.27 ± 0.39	**97.93 ± 0.37**
Dataset 3	75.91 ± 1.08	88.64 ± 0.75	87.31 ± 0.81	85.06 ± 0.72	89.27 ± 0.69	86.37 ± 0.78	88.54 ± 0.62	90.37 ± 0.51	**93.14 ± 0.42**
Dataset 4	97.61 ± 0.35	98.15 ± 0.32	98.07 ± 0.33	98.32 ± 0.29	98.81 ± 0.26	98.73 ± 0.27	99.08 ± 0.27	99.19 ± 0.25	**99.79 ± 0.26**
Dataset 5	97.69 ± 0.36	98.24 ± 0.33	98.39 ± 0.31	98.71 ± 0.26	98.82 ± 0.28	98.84 ± 0.26	99.21 ± 0.23	99.26 ± 0.25	**99.84 ± 0.23**
Dataset 6	97.73 ± 0.32	98.42 ± 0.29	98.57 ± 0.28	99.14 ± 0.29	99.08 ± 0.31	99.06 ± 0.26	99.29 ± 0.21	99.37 ± 0.26	**99.91 ± 0.22**
Dataset 7	97.53 ± 0.37	98.04 ± 0.32	98.19 ± 0.33	98.84 ± 0.28	99.08 ± 0.30	99.16 ± 0.21	99.10 ± 0.31	99.07 ± 0.28	**99.37 ± 0.25**
Dataset 8	97.49 ± 0.37	98.09 ± 0.32	98.22 ± 0.36	98.81 ± 0.29	99.17 ± 0.31	99.21 ± 0.32	99.11 ± 0.32	99.14 ± 0.29	**99.49 ± 0.27**
Dataset 9	97.51 ± 0.38	98.10 ± 0.33	98.29 ± 0.35	98.79 ± 0.32	99.17 ± 0.29	99.20 ± 0.32	99.24 ± 0.29	99.23 ± 0.31	**99.71 ± 0.28**
Average	93.87	96.83	96.84	96.90	97.57	97.30	97.78	97.89	**98.73**
Methods	DBN	MSIDBN	MSICNN	IMGCN	CVC-Net	A-TSGNN	MCFormer	I^2SGCN	Ours

* The bold fonts mean the highest performance.
** ± means the standard deviation.
*** The experimental results for each method were repeated 10 times, and the corresponding standard deviations were computed.

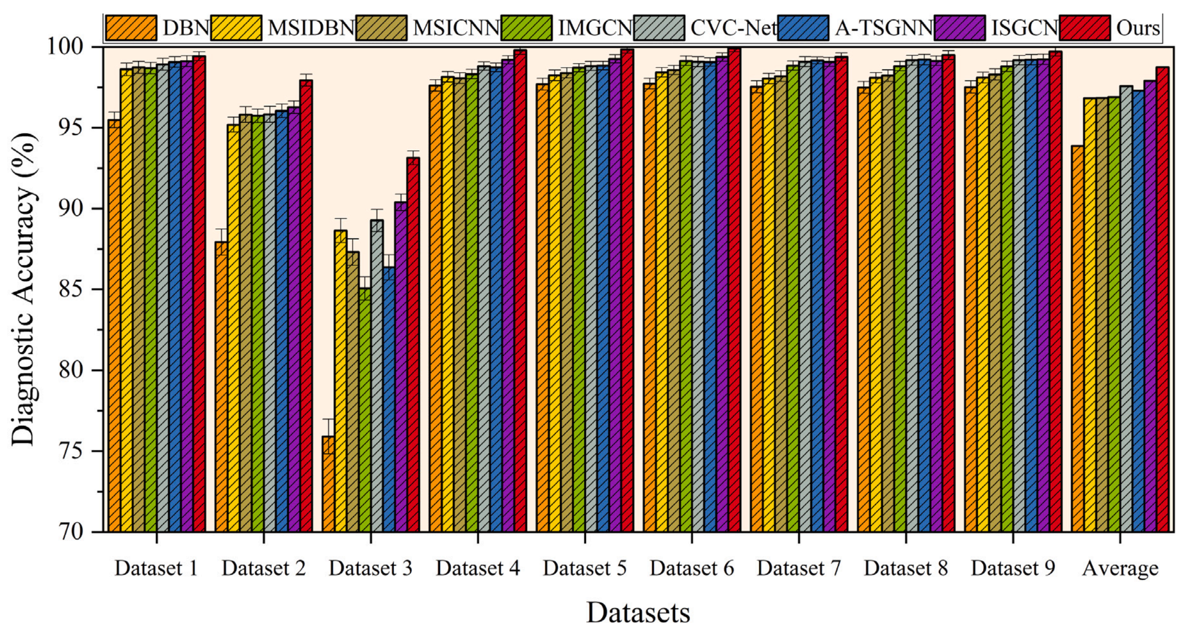

Fig. 19. Diagnostic results for various methods.

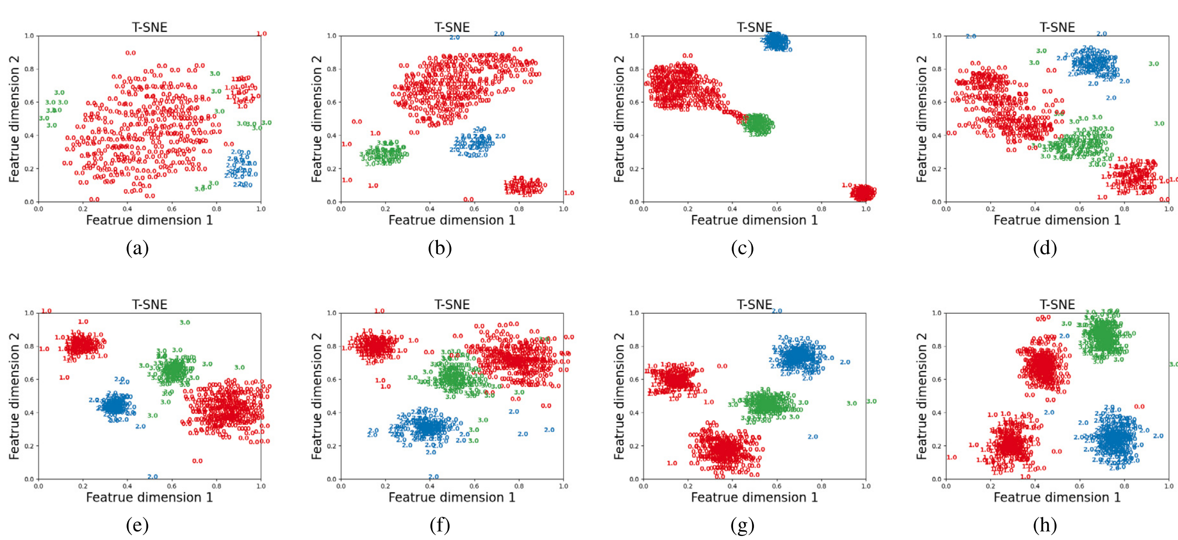

Fig. 20. Feature visualization on Dataset 6 in Case Study 2. (a) DBN; (b) MSIDBN; (c) MSICNN; (d) IMGCN; (e) CVC-Net; (f) A-TSGNN; (g) I^2SGCN; (h) Ours.

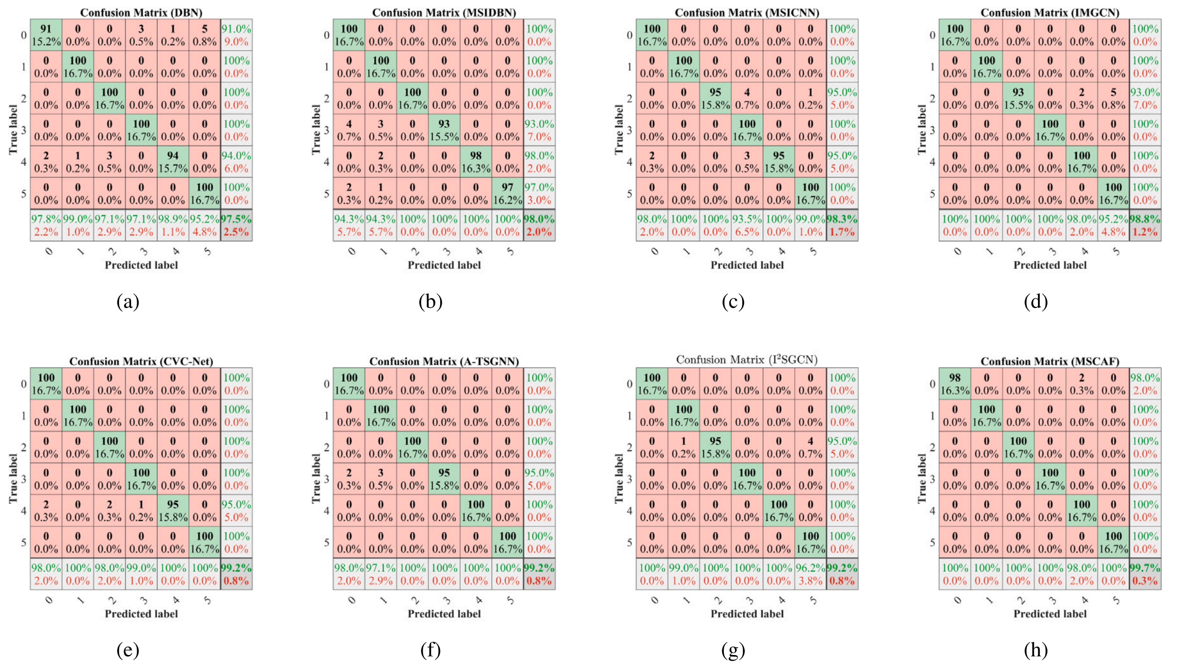

Fig. 21. Confusion matrix results on Dataset 8 in Case Study 3. (a) DBN; (b) MSIDBN; (c) MSICNN; (d) IMGCN; (e) CVC-Net; (f) A-TSGNN; (g) I^{2}SGCN; (h) Ours.

where true positives (TP), true negatives (TN), false positives (FP), and false negatives (FN) refer to the correctly predicted positive samples, correctly predicted negative samples, incorrectly predicted positive samples, and incorrectly predicted negative samples, respectively. Therefore, the confusion matrix results for different methods are shown in Fig. 21.

It can be seen that our proposed method has a higher fault diagnosis accuracy. Specifically, two samples from Label 0 were misclassified as Label 4. In contrast, the worst-performance method (i.e., DBN) has the lowest fault identification performance, including Label 0 and Label 4. Therefore, the proposed multi-source sensor correlation adaptive fusion framework effectively integrates uncertainty quantification to enhance fault diagnosis. It can provide more representative fault information, which can facilitate the accurate identification of different health conditions.

Second, the Receiver Operating Characteristic (ROC) curve is further conducted to test the performance of methods in this work across various threshold settings. It can plot the TPR against FPR, which can illustrate the trade-off between correctly identifying positive samples and negative samples. The ROC results are represented in Fig. 22.

The results in Fig. 22 demonstrated that our MSCAF can achieve a maximum area under the curve (AUC) of class 1 and class 2, which indicates the optimal diagnostic performance with high sensitivity and specificity. Hence, the proposed MSCAF with uncertainty quantification can effectively identify each health condition and show excellent stability.

5. Model discussion

5.1. Ablation experiments

To show the contributions of one major component (i.e., feature extractor) and two main innovations of the proposed MSCAF (i.e., uncertainty quantification and SpS). Therefore, four variants were further developed from the proposed MSCAF, namely: (1) method 1 (**M1**): Only a simple ANN is used to replace the CNN and GCN as the feature extractor, (2) method 2 (**M2**): a majority vote mechanism is employed to achieve multi-source sensor fusion instead of using uncertainty quantification and SpS, (3) method 3 (**M3**): MSCAF without uncertainty quantification, and (4) method 4 (**M4**): MSCAF without SpS. The diagnostic results and inference times of four model variants across three different datasets (i.e., Dataset3, Dataset6, and Dataset9) for three case studies are presented in Table 10.

It can be seen from the data in Table 10 that our proposed method consistently outperforms the four variants in terms of accuracy and standard metrics. Specifically, MSCAF outperforms **M1**, **M2**, **M3**, and **M4** by 0.54%, 2.1%, 1.7%, and 0.95%, respectively. These significant improvements suggested that incorporating uncertainty quantification and SpS into multi-source sensor fusion fault diagnosis is crucial. Hence, the proposed method with uncertainty quantification consistently yields better diagnostic results than label-level fusion methods (e.g., traditional multi-source sensor fusion). In addition, SpS is crucial, and assigning significantly smaller weights to unreliable views can prevent them from misguiding the final fault diagnosis. While our proposed method introduces approximately 1–3 s of additional processing time compared to other methods, it yields a satisfactory improvement in diagnostic accuracy. We believe this trade-off is justified given the critical nature of fault diagnosis applications, where diagnostic accuracy is of paramount importance. Moreover, the computational burden can be alleviated with the advancements in software and hardware technologies.

5.2. Analysis of noise resistance

As noise increases, the signals measured by multi-source sensors may become unclear, which negatively affects the accuracy of fault diagnosis. If the influence of noise is accounted for, it may result in correct fault type identification. Therefore, investigating methods to handle noise and uncertainties is crucial to improving the reliability of fault diagnosis, particularly in real-world operating environments. Therefore, in this work, we evaluated the robustness of all methods, except for DBN, by introducing varying levels of Gaussian white noise, Rayleigh noise, and Bernoulli noise into the multi-source sensor signals. So, the signal-to-noise ratio (SNR) is introduced to represent the noise level and is defined as follows:

$$SNR = 10\log_{10}(P_o/P_n) \tag{45}$$

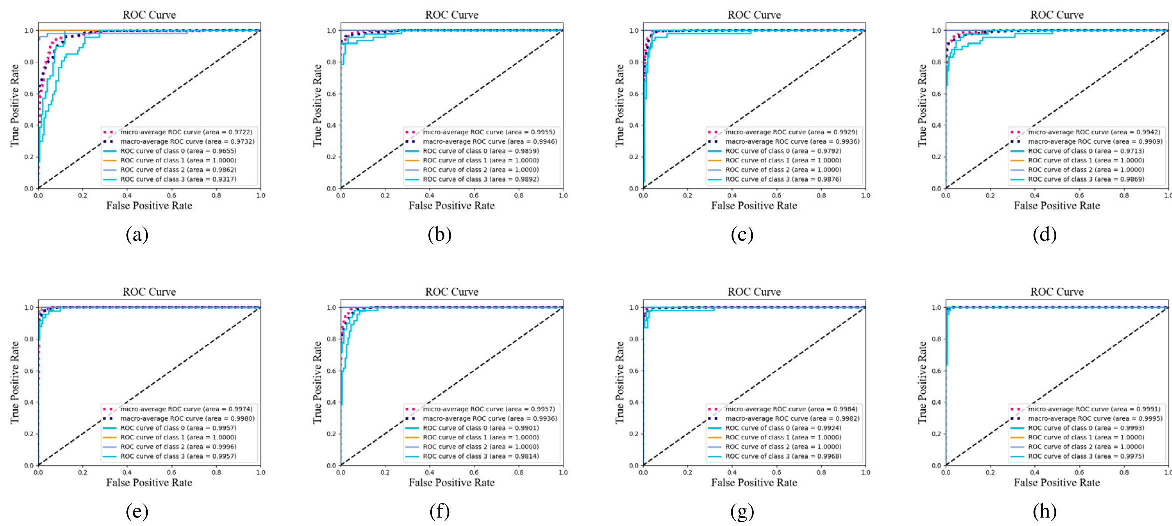

Fig. 22. ROC curves on Dataset 4 in Case Study 2. (a) DBN; (b) MSIDBN; (c) MSICNN; (d) IMGCN; (e) CVC-Net; (f) A-TSGNN; (g) I^{2}SGCN; (h) Ours.

Table 10
Experimental results and inference time of ablation experiments.

Method	Dataset 3		Dataset 6		Dataset 9	
	Accuracy	Inference time	Accuracy	Inference time	Accuracy	Inference time
M1	92.64 ± 0.46%	1.74 ± 0.25 s	99.37 ± 0.17%	1.65 ± 0.22 s	99.17 ± 0.28%	1.82 ± 0.35 s
M2	91.16 ± 0.42%	2.28 ± 0.35 s	97.81 ± 0.24%	2.19 ± 0.32 s	97.64 ± 0.36%	2.37 ± 0.45 s
M3	91.58 ± 0.48%	3.03 ± 0.42 s	98.21 ± 0.19%	2.91 ± 0.38 s	98.03 ± 0.34%	3.12 ± 0.55 s
M4	92.25 ± 0.43%	3.71 ± 0.58 s	98.96 ± 0.17%	3.62 ± 0.52 s	98.76 ± 0.35%	3.84 ± 0.68 s
MSCAF	93.14 ± 0.42%	4.43 ± 0.75 s	99.91 ± 0.08%	4.34 ± 0.72 s	99.71 ± 0.28%	4.52 ± 0.85 s

where P_o and P_n stand for the power of original multi-source sensor signals and the power of added noise, respectively. The diagnostic radar maps under varying noise levels, ranging from −10 dB to 0 dB, for three different datasets (i.e., Dataset 3, Dataset 6, and Dataset 9) are shown in Fig. 23.

The diagram shows that the diagnostic performance of all methods decreases synchronously as the SNR reduces; however, the robustness of our proposed network against different noises is higher than that of MSIDBN, MSICNN, IMGCN, CVC-Net, A-TSGNN, I^{2}SGCN and IMCGCN. Specifically, on Dataset 9, the proposed method achieves diagnostic accuracies of 99.45%, 99.19%, 97.86%, 96.63%, 93.27%, and 91.59% under different levels of Gaussian white noise. This demonstrates that uncertainty quantification and SpS are crucial at different noise levels, as they ensure outstanding diagnostic performance.

5.3. Loss and accuracy curves

To observe the overall performance of different methods in terms of diagnosis and learning progress, the loss and accuracy curves of all the methods can be illustrated in Fig. 24.

The graphs above show that the proposed MSCAF achieves maximum accuracy more efficiently and maintains stability compared to other SOTA methods. Meanwhile, the proposed method effectively suppresses oscillating loss during the training process, which can result in a smoother loss curve and faster convergence speed. It indicates that our proposed method not only effectively alleviates loss fluctuations but also improves the convergence speed of network training.

5.4. Statistical test

The Friedman test, a non-parametric statistical test (Friedman Test, F_t), is employed across multiple diagnostic tasks to further illustrate the differences among the various methods. First, we proposed two hypotheses: (1) Null Hypothesis (H_0): There are no differences among these methods; (2) Alternative Hypothesis (H_1): There is at least one significant difference among these methods. Second, we ranked the average scores (i.e., accuracies) for each method across all the tasks, as given in Table 11.

Table 11
Average ranks for each diagnostic task across different methods.

	DBN	MSIDBN	MSICNN	IMGCN	CVC-Net	A-TSGNN	I^{2}SGCN	Ours
Average rank	8	6.556	5.778	5.222	3.556	3.444	2.444	1

Third, we calculated the Friedman statistic, χ_F^2, based on these ranks.

$$\chi_F^2 = \frac{12}{nk(k+1)} \sum_{j=1}^{k} \left(R_j - \frac{n(k+1)}{2} \right)^2 \tag{46}$$

where k means the number of methods. n represents the number of all tasks in this work. R_j indicates the average ranks for each method.

Finally, we compared the calculated $\chi_F^2 = 60.7836$ value to the chi-square distribution table with degrees of freedom $k - 1 = 8 - 1 = 7$ to determine that there was a statistically significant difference among all methods. A Critical Difference (CD) diagram, often used with the F_t, is employed to represent multiple pairwise comparisons among the various models visually. After the Friedman test showed significance, the Nemenyi post-hoc test was conducted to calculate the Critical Difference (CD), as depicted in Fig. 25.

It can be observed that the methods CVC-Net, A-TSGNN, I^{2}SGCN, and MSCAF are connected because their rank difference is less than the CD of 3.1061, which can indicate no significant performance difference. In contrast, the methods DBN, MSIDBN, MSICNN, and IMGCN are not connected, which can show a statistically significant difference in performance.

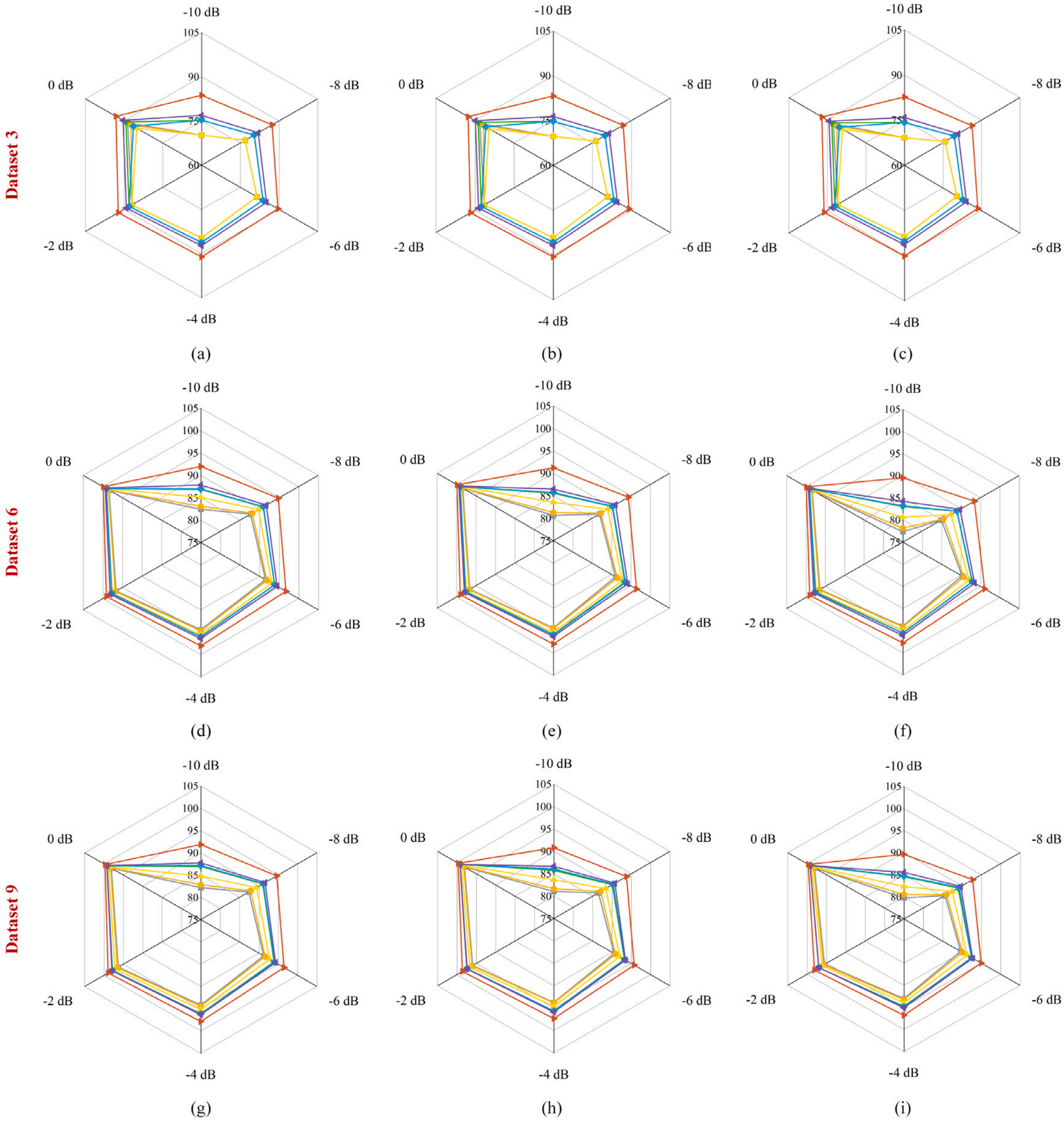

Fig. 23. Accuracy of different models on Dataset 9 under varying levels of noise.

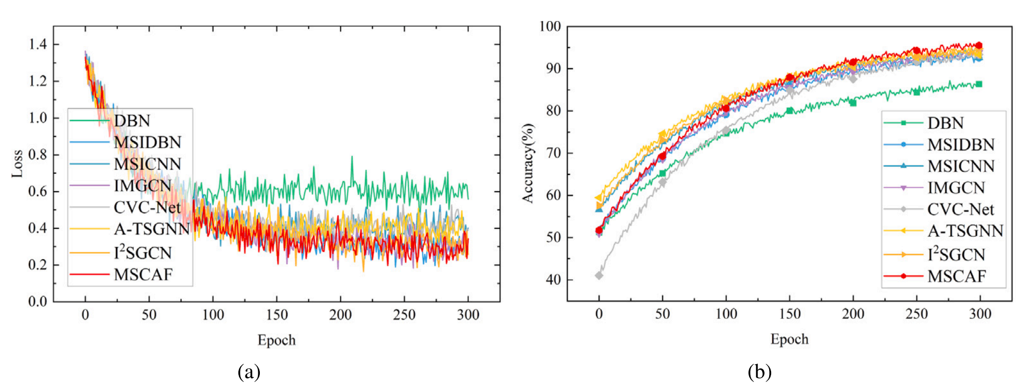

Fig. 24. Loss and accuracy curves of different methods. (a) Loss curve; (b) Accuracy curve.

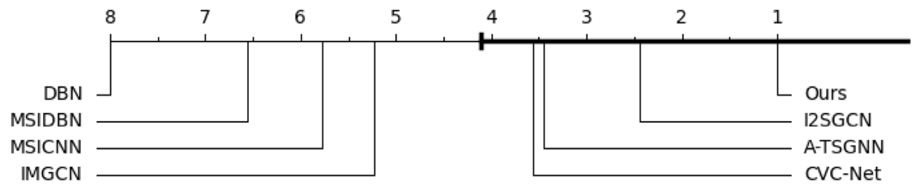

Fig. 25. CD diagram of average rank on the ranking axis.

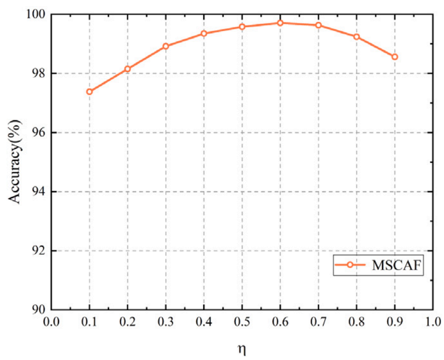

Fig. 26. The sensitivity of the proposed MSCAF to the hyperparameter η on Dataset 9.

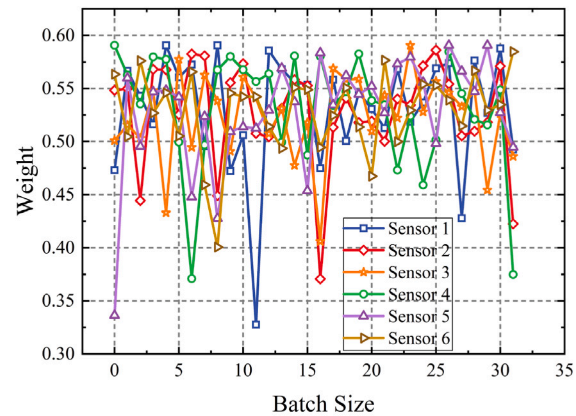

Fig. 27. Visualization of Uncertainty and Confidence Levels.

5.5. Hyperparameter sensitivity analysis

To evaluate the impact of the temperature hyperparameter η on the performance of the proposed MSCAF method, we conducted a sensitivity analysis on Dataset 9, as shown in Fig. 26.

As illustrated in Fig. 26, the model demonstrates stable performance across a broad range of η values, with accuracy gradually increasing and peaking at $\eta = 0.6$. This indicates that a moderate temperature factor η positively contributes to the adaptability of our proposed MSCAF. However, setting η too low or too high results in slight diagnostic performance drops due to insufficient or excessive emphasis on correlation.

5.6. Visualization of uncertainty and confidence levels

To visually and quantitatively analyze the adaptive weights assigned to each sensor based on their associated uncertainty and confidence levels, we visualize the weight distributions of six sensors across different samples from Dataset 4 throughout the training process, as illustrated in Fig. 27.

As shown in Fig. 27, the weights assigned to sensors vary across different samples, thereby enabling reliable fusion based on uncertainty quantification. Specially, Sensors 1 and 2 consistently receive higher weights, suggesting greater reliability or lower uncertainty compared to the others.

6. Conclusion

This paper first explored a novel multi-source sensors correlation adaptive fusion framework for quantifying uncertainty. We employed the feature extractor to obtain category probabilities from multi-source sensors and combined the Dempster–Shafer (DS) theory and Dirichlet distribution to quantify uncertainties. Compared to traditional multi-source sensor fusion methods, our proposed MSCAF effectively reduces the computational complexity of uncertainty quantification and is also compatible with existing DL-based models for intelligent fault diagnosis. We proposed to split low-confidence and high-confidence sensors by assessing different levels of correlation. The reward and penalty functions were introduced to deal with conflict sensors and enable reliable fusion. Based on its robust performance and promising potential demonstrated in case studies, the proposed method could be valuable for gaining researchers' trust in DL-based models with uncertainty quantification for intelligent fault diagnosis. Experimental results indicate that the proposed MSCAF achieves an average diagnostic performance of 99.42 ± 0.27%, 97.93 ± 0.37%, 93.14 ± 0.42%, 99.79 ± 0.26%, 99.84 ± 0.23%, 99.91 ± 0.22%, 99.37 ± 0.25%, 99.49 ± 0.27%, and 99.71 ± 0.28% across nine datasets, thereby validating its applicability and superiority with uncertainty quantification.

7. Future works

(1) Although the proposed method can effectively quantify uncertainty, it overlooks epistemic uncertainty. In the future, we plan to enhance the existing model in three ways. First, we aim to introduce post-hoc interpretability to "black-box" models, such as DL-based diagnostic models. Second, we will integrate expert knowledge with our approach and address exceptional cases that current DL-based models cannot handle through manual intervention. Lastly, we will conduct traceability analysis based on uncertainty quantification to identify the sources of uncertainty, further refining the model [41].

(2) In many real industrial scenarios, signals collected by sensors are distributed across multiple locations or mechanical equipment, and centralizing it can be impractical or raise security concerns. Hence, it is necessary to introduce federated learning into the proposed method to enable collaborative model training across distributed data sources without compromising data privacy. This improvement approach not only enhances the robustness and generalization capability of our proposed method under variable operating conditions but also meets privacy regulations, which can make it particularly valuable for cross-organizational or sensitive industrial applications [42].

(3) To enable efficient real-time monitoring and fault diagnosis with low computational costs and rapid response, the proposed MSCAF

need to be designed as a lightweight framework with reduced reliance on cloud-based transmission. This framework can enhance diagnostic responsiveness, lower energy consumption, and improve data privacy in the future [43].

(4) In practical circumstances, the variability of working conditions and the unpredictability of different health conditions will lead to the unknown categories in the testing dataset. Therefore, we need to acknowledge the significance of generalization to unknown faults in industrial diagnostic systems. Drawing inspiration from [44], we will explore meta-learning strategies to enhance the generalization performance to quickly adapt to unknown fault categories.

CRediT authorship contribution statement

Yue Yu: Writing – original draft, Validation, Software, Resources, Methodology, Investigation, Formal analysis, Data curation, Conceptualization. **Hamid Reza Karimi:** Writing – review & editing, Visualization, Supervision, Project administration, Conceptualization. **Len Gelman:** Writing – review & editing, Validation, Methodology, Investigation. **Jinghui Tian:** Writing – review & editing, Validation, Methodology, Investigation. **Peng Mei:** Writing – review & editing, Validation, Methodology, Investigation.

Declaration of competing interest

We declare that we do not have any commercial or associative interest that represents a conflict of interest in connection with the work submitted.

Acknowledgments

This work was funded in part by the China Scholarship Council (CSC) under Grant No. N202308130067, the Horizon Marie Sklodowska-Curie Actions Program (Grant No. 101073037), the China Postdoctoral Science Foundation, China (Grant No. 2024M754076), and the Italian Ministry of University and Research under the grant 'Learning-based Model Predictive Control by Exploration and Exploitation in Uncertain Environments' (PRIN PNRR 2022 fund, Grant ID P2022EXP2W).

Data availability

The code and model are available at: https://github.com/Polimi-YuYue/Polimi-YuYue. The authors do not have permission to share private data.

References

[1] Ren X, Zhao W, Liu M, Wang S, Shao H, Zhao K. Multi-source domain self-supervised enhanced transfer fault diagnosis approach with source sample refinement strategy. Reliab Eng Syst Saf 2024;251:110380.

[2] Yu Y, Karimi HR, Gelman L, Liu X. A novel digital twin-enabled three-stage feature imputation framework for non-contact intelligent fault diagnosis. Adv Eng Informatics 2025;66:103434.

[3] Zhang Y, Han D, Shi P. Semi-supervised prototype network based on compact-uniform-sparse representation for rotating machinery few-shot class incremental fault diagnosis. Expert Syst Appl 2024;255:124660.

[4] Kong X, Cai B, Zou Z, Wu Q, Wang C, Yang J, Wang B, Liu Y. Three-model-driven fault diagnosis method for complex hydraulic control system: Subsea blowout preventer system as a case study. Expert Syst Appl 2024;247:123297.

[5] Qin Y, Liu H, Wang Y, Mao Y. Inverse physics–informed neural networks for digital twin–based bearing fault diagnosis under imbalanced samples. Knowl-Based Syst 2024;292:111641.

[6] Yu Y, Karimi HR, Gelman L, Cetin AE. MSIFT: A novel end-to-end mechanical fault diagnosis framework under limited & imbalanced data using multi-source information fusion. Expert Syst Appl 2025;274:126947.

[7] Sun R-B, Ren H, Yang Z-B, Chen X. Wind turbine fault diagnosis based on cyclostationary feature detection from compressive samples. IEEE Sensors J 2024.

[8] Xu X, Ou X, Ge L, Qiao Z, Shi P. Simulated data-assisted fault diagnosis framework with dual-path feature fusion for rolling element bearings under incomplete data. IEEE Trans Instrum Meas 2025.

[9] Kong D, Huang W, Zhao L, Ding J, Wu H, Yang G. Mining knowledge from unlabeled data for fault diagnosis: A multi-task self-supervised approach. Mech Syst Signal Process 2024;211:111189.

[10] Liu R, Ding X, Wu Q, He Q, Shao Y. An interpretable multiplication-convolution network for equipment intelligent edge diagnosis. IEEE Trans Syst Man, Cybern: Syst 2024.

[11] Ma K, Yang J, Liu P. Relaying-assisted communications for demand response in smart grid: Cost modeling, game strategies, and algorithms. IEEE J Sel Areas Commun 2019;38(1):48–60.

[12] Ding J, Wang Y, Qin Y, Tang B. Multi-objective optimal deep deconvolution and its application to early fault signal enhancement of rotating machineries. Mech Syst Signal Process 2024;221:111722.

[13] Wang C, Yang J, Jie H, Tian B, Zhao Z, Chang Y. An uncertainty perception metric network for machinery fault diagnosis under limited noisy source domain and scarce noisy unknown domain. Adv Eng Informatics 2024;62:102682.

[14] Wang C, Tian B, Yang J, Jie H, Chang Y, Zhao Z. Neural-transformer: A brain-inspired lightweight mechanical fault diagnosis method under noise. Reliab Eng Syst Saf 2024;251:110409.

[15] Das L, Gjorgiev B, Sansavini G. Uncertainty-aware deep learning for monitoring and fault diagnosis from synthetic data. Reliab Eng Syst Saf 2024;251:110386.

[16] Ren J, Wen J, Zhao Z, Yan R, Chen X, Nandi AK. Uncertainty-aware deep learning: A promising tool for trustworthy fault diagnosis. IEEE/CAA J Autom Sin 2024;11(6):1317–30.

[17] Lu H, Thelen A, Fink O, Hu C, Laflamme S. Federated learning with uncertainty-based client clustering for fleet-wide fault diagnosis. Mech Syst Signal Process 2024;210:111068.

[18] Zhang X, Wang C, Zhou W, Xu J, Han T. Trustworthy diagnostics with out-of-distribution detection: A novel max-consistency and min-similarity guided deep ensembles for uncertainty estimation. IEEE Internet Things J 2024.

[19] Liu Z, Deveci M, Pamučar D, Pedrycz W. An effective multi-source data fusion approach based on α-divergence in belief functions theory with applications to air target recognition and fault diagnosis. Inf Fusion 2024;110:102458.

[20] Xu H, Wang X, Huang J, Zhang F, Chu F. Semi-supervised multi-sensor information fusion tailored graph embedded low-rank tensor learning machine under extremely low labeled rate. Inf Fusion 2024;105:102222.

[21] Han T, Li Y-F. Out-of-distribution detection-assisted trustworthy machinery fault diagnosis approach with uncertainty-aware deep ensembles. Reliab Eng Syst Saf 2022;226:108648.

[22] Sensoy M, Kaplan L, Kandemir M. Evidential deep learning to quantify classification uncertainty. Adv Neural Inf Process Syst 2018;31.

[23] Han Z, Zhang C, Fu H, Zhou JT. Trusted multi-view classification with dynamic evidential fusion. IEEE Trans Pattern Anal Mach Intell 2022;45(2):2551–66.

[24] Zhang K, Li H, Cao S, Lv S, Yang C, Xiang W. Trusted multi-source information fusion for fault diagnosis of electromechanical system with modified graph convolution network. Adv Eng Informatics 2023;57:102088.

[25] Xu C, Zhao W, Zhao J, Guan Z, Song X, Li J. Uncertainty-aware multiview deep learning for internet of things applications. IEEE Trans Ind Informatics 2022;19(2):1456–66.

[26] Wang Z, Luo Q, Chen H, Zhao J, Yao L, Zhang J, Chu F. A high-accuracy intelligent fault diagnosis method for aero-engine bearings with limited samples. Comput Ind 2024;159:104099.

[27] Li Q, Liu Y, Sun S, Qin Z, Chu F. Deep expert network: A unified method toward knowledge-informed fault diagnosis via fully interpretable neuro-symbolic AI. J Manuf Syst 2024;77:652–61.

[28] Wang X, Chen H, Zhao J, Song C, Zhang Y, Yang Z-X, Wong PK. Wind turbine fault diagnosis for class-imbalance and small-size data based on stacked capsule autoencoder. IEEE Trans Ind Informatics 2024.

[29] Defferrard M, Bresson X, Vandergheynst P. Convolutional neural networks on graphs with fast localized spectral filtering. Adv Neural Inf Process Syst 2016;29.

[30] Kipf TN, Welling M. Semi-supervised classification with graph convolutional networks. 2016, arXiv preprint arXiv:1609.02907.

[31] Wan P, Zhang S, Shao W, Zhao J, Yang Y, Kong W, Xue H, Zhang D. Correlation-adaptive multi-view CEUS fusion for liver cancer diagnosis. In: International conference on medical image computing and computer-assisted intervention. Springer; 2024, p. 188–97.

[32] Zhang X, Liu J, Zhang X, Lu Y. Multiscale channel attention-driven graph dynamic fusion learning method for robust fault diagnosis. IEEE Trans Ind Informatics 2024.

[33] Mirzadeh I, Alizadeh K, Mehta S, Del Mundo CC, Tuzel O, Samei G, Rastegari M, Farajtabar M. Relu strikes back: Exploiting activation sparsity in large language models. 2023, arXiv preprint arXiv:2310.04564.

[34] Yu Y, Shi P, Tian J, Xu X, Hua C. Rolling mill health states diagnosing method based on multi-sensor information fusion and improved DBNs under limited datasets. ISA Trans 2023;134:529–47.

[35] Shi P, Yu Y, Gao H, Hua C. A novel multi-source sensing data fusion driven method for detecting rolling mill health states under imbalanced and limited datasets. Mech Syst Signal Process 2022;171:108903.

[36] Yang C, Liu J, Zhou K, Jiang X, Zeng X. An improved multi-channel graph convolutional network and its applications for rotating machinery diagnosis. Measurement 2022;190:110720.

[37] Li X, Wang Y, Yao J, Li M, Gao Z. Multi-sensor fusion fault diagnosis method of wind turbine bearing based on adaptive convergent viewable neural networks. Reliab Eng Syst Saf 2024;245:109980.

[38] Wang Z, Wu Z, Li X, Shao H, Han T, Xie M. Attention-aware temporal–spatial graph neural network with multi-sensor information fusion for fault diagnosis. Knowl-Based Syst 2023;278:110891.

[39] Li X, Xiao S, Li Q, Zhu L, Wang T, Chu F. The bearing multi-sensor fault diagnosis method based on a multi-branch parallel perception network and feature fusion strategy. Reliab Eng Syst Saf 2025;261:111122.

[40] Yu Y, He Y, Karimi HR, Gelman L, Cetin AE. A two-stage importance-aware subgraph convolutional network based on multi-source sensors for cross-domain fault diagnosis. Neural Netw 2024;179:106518.

[41] Dong Y, Jiang H, Wang X, Mu M, Jiang W. An interpretable multiscale lifting wavelet contrast network for planetary gearbox fault diagnosis with small samples. Reliab Eng Syst Saf 2024;251:110404.

[42] Wen T, Chen X, Zhang D, Roberts C, Cai B. A sequential and asynchronous federated learning framework for railway point machine fault diagnosis with imperfect data transmission. IEEE Trans Ind Informatics 2024.

[43] Wang C, Yang J, Jie H, Tao Z, Zhao Z. A lightweight progressive joint transfer ensemble network inspired by the Markov process for imbalanced mechanical fault diagnosis. Mech Syst Signal Process 2025;224:111994.

[44] Wang C, Shu Z, Yang J, Zhao Z, Jie H, Chang Y, Jiang S, See KY. Learning to imbalanced open set generalize: A meta-learning framework for enhanced mechanical diagnosis. IEEE Trans Cybern 2025.